CR-152396
(W. Johnson)

SCI (Vt) AERONAUTICAL & MARINE SYSTEMS DIVISION
SYSTEMS CONTROL, INC. (Vt) ■ 1801 PAGE MILL ROAD ■ PALO ALTO, CA 94304 ■ TELEX 348-433 ■ (415) 494-1165

JULY 1980

TR 6419-01

DYNAMIC MODAL ESTIMATION USING INSTRUMENTAL VARIABLES

Prepared by
H. Salzwedel

Prepared for
NASA-AMES RESEARCH CENTER
Moffett Field, California

FOREWORD

A method to determine the modes of dynamical systems is described. The inputs and outputs of a system are Fourier transformed and averaged to reduce the error level. An instrumental variable method that estimates modal parameters from multiple correlations between responses of single input, multiple output systems is applied to estimate aircraft, spacecraft, and off-shore platform modal parameters.

TABLE OF CONTENTS

		Page
I.	INTRODUCTION	1
II.	INSTRUMENTAL VARIABLES ALGORITHM	3
III.	MODEL ORDER DETERMINATION	7
IV.	EXAMPLES OF INSTRUMENTAL VARIABLE MODAL ESTIMATION APPLICATIONS	9
	4.1 Application of the Modal Estimation Algorithm to B-52 Flight Test Data	9
	4.2 Application of the IVME Algorithm to Identify the Dynamics of the Boeing 747 - Space Shuttle Combination	12
	4.3 Application of the AVME Algorithm to Off-Shore Platform Data	29
	4.4 Application of the IVME Algorithm to Space-Structure Modal Estimation	31
V.	CONCLUSIONS	55
REFERENCES		57
APPENDIX A:	FREQUENCY DOMAIN ARMA EQUATIONS	59
APPENDIX B:	SOLUTION OF THE INSTRUMENTAL VARIABLES ARMA EQUATIONS	61
APPENDIX C:	AVERAGING SOLUTION OF THE INSTRUMENTAL VARIABLES ARMA EQUATIONS	63

I. INTRODUCTION

A major task in the development of structures (ground structures, aircraft and spacecraft) and their control systems is the identification and demonstration of satisfactory dynamic characteristics.Each specific structural system, however, has unique characteristics which require special analytical treatment. For the development of aircraft, it is not only necessary to determine its flutter boundary or establish that the aircraft is flutter-free throughout its operating envelope; it is also desirable to obtain detailed information about dynamic characteristics such as aircraft gust response and provide data for the verification of mathematical models of the aircraft. The determination of the dynamic characteristics of off-shore platforms is essential for the verification of their safety in different sea states. The modes of large space structures are very close to each other, and it is necessary to identify them very accurately not to excite them inadvertently by the control system [1,2]. The most important parameters are generally those defining the frequency and damping of the low-damped modes of the system. A number of surveys show the development of stability testing of aircraft [3-7]. These procedures typically involve fast sine-sweep excitations and analysis of the response. In Refs. 8 and 9, methods for the identification of frequencies and mode shapes of off-shore platforms have been developed. These methods are based on the maximum entropy spectral analysis method [10].

Testing of the dynamic characteristics of systems involve three tasks: design of an excitation input that excites all significant modes, measuring the response of the system, and then extracting the modal parameters from the response. In Ref. 11, it was shown that the best accuracy in modal parameters can be obtained for a given amount of data by exciting the system by an

external input in the required frequency band and measuring the system transfer function.

Testing methods, such as fast sine-sweep measurement of the transfer funtion and measuring the transient decay after an impulse input, rely on a high signal-to-noise ratio and obtain an accurate response measurement in a laboratory environment [11]. The errors of these measurements have only small correlations and can be considered to be white. In-flight tests of the measured accelerations and moments of aircraft are not only the response to excitation inputs of the control surfaces, but also to gust inputs. The gust responses are necessarily non-Gaussian distributed and highly correlated. In Refs. 13 and 14, it was shown that the least squares estimates are very sensitive to the Gaussian assumption and the mean estimate is much more robust. Reference 11 shows an example, where correlating the response and a measured external input, as well as averaging reduces the test time, for a given level of accuracy by a factor of 10 to 15. Reference 15 combines the robustness of the single-input/ single-output method of Ref. 11 with the multi-input/multi-output method of Ref. 12 to design a robust and highly efficient method for flutter testing. The robustness of this algorithm is due to averaging of the autospectra of different measurements. References 11 and 16 show that the autospectra, as well as the cross spectra of measured outputs contain information about the modal parameters of the test structure.

This report is concerned with estimating modal parameters by combining autospectra and cross-spectra of responses for different time delays. In the following sections, a frequency domain derivation of an instrumental variable algorithm is shown. Four examples of its application to modal parameter estimates of aircraft, an off-shore platform, and a simulated space structure are presented.

II. INSTRUMENTAL VARIABLES ALGORITHM

The input/output relation of a system can be described to first order by

$$y = X\theta + v \tag{2.1}$$

where y and X are measured data, θ are the system parameters to be identified, and v is some zero mean noise term which is assumed to be white. The least squares estimate of θ is

$$\theta_{LS} = (X^T X)^{-1} X^T y \tag{2.2}$$

$$E[\theta_{LS}] = \theta + (X^T X)^{-1} E[Xv].$$

The least squares estimate, therefore, has a bias of the measurments X and the noise v are correlated. In the instrumental variables method Eq. (2.1) is premultiplied by a matrix $[Z \mid \text{rank } Z = \text{rank } X]$ that is not correlated with v. Hence, the instrumental variables estimate of θ,

$$\theta_{IV} = (Z^T X)^{-1} Z^T y,$$

$$E[\theta_{IV}] = \theta \tag{2.3}$$

is unbiased. In the present case, we use for instrumental variables measurements of a past time. Choosing a time delay, τ, sufficiently large these measurements are not correlated with the noise of the current ones.

The input/output relationship of a linear time-invariant dynamic system can be modeled by a set of linear constant coefficient differential equations (Appendix A). In the frequency domain these equations may be written as

$$(j\omega)^n Y_o = Y_o [(j\omega)^{n-1}, \ldots, 1]\alpha + \beta^T \begin{bmatrix} (j\omega)^m \\ \vdots \\ 1 \end{bmatrix} U_o \tag{2.4}$$

where

$$\alpha = [-a_n , \ldots, -a_1]^T ,$$

$$\beta = [b_m, \ldots, b_1]^T$$

are the coefficients of the characteristic polynomials for poles and zeros, respectively [12], and Y_o and U_o are the Fourier transforms of output and input, $[y(t), u(t) | 0 \leq t \leq T]$.

In Refs. 12 and 15, Eq. (2.4) was premultiplied by

$$[(-j\omega)^{n-1} \ \ldots \ 1]^T \ Y_o^{T*} \ e^{j\omega\tau}$$

to get a set of independent equations. Due to the ω-dependent phase of $Y_o^{T*}e^{j\omega\tau}$, this causes some frequencies to be weighted more heavily than others and is the reason for some of the difficulties in estimating ARMA parameters for finite data sets. By premultiplying Eq. (2.4) instead by the instrumental variable,

$$[(-j\omega)^{n-1} \ldots 1]^T \ Y_{-\tau}^{T*} \ e^{j\omega\tau},$$

$$Y_{-\tau} = F[y(t-\tau) | -\tau \leq t \leq T-\tau],$$

the undesirable frequency weighting is avoided. This follows from the fact that

$$E[Y_o] = E[Y_{-\tau} \ e^{j\omega\tau}]$$

for a stationary system. Premultiplying Eq. (2.4) with

$$U_o^*[(-j\omega)^m \ldots 1]^T$$

gives an additional independent equation for each of the p outputs. The resulting equations are shown in Appendix A.

There are several methods available to solve the instrumental variables ARMA equations; some of which include least squares, averaging, maximum likelihood and prediction error methods. The maximum likelihood method and the prediction error method generally give the best fit but their complexity and computation requirements make them unsuited for on-line applications. The

least squares and averaging methods are fast and well suited for on-line applications [15].

The least squares method of Appendix B estimates ARMA models that fit the measured spectra very well, but is very sensitive to non-Gaussian noise and spurious peaks in the spectra. The averaging method of Appendix C reduces the parameter uncertainty for small data sets, but increases the fit error. A flowchart of an on-line application of this algorithm is shown in Figure 2.1.

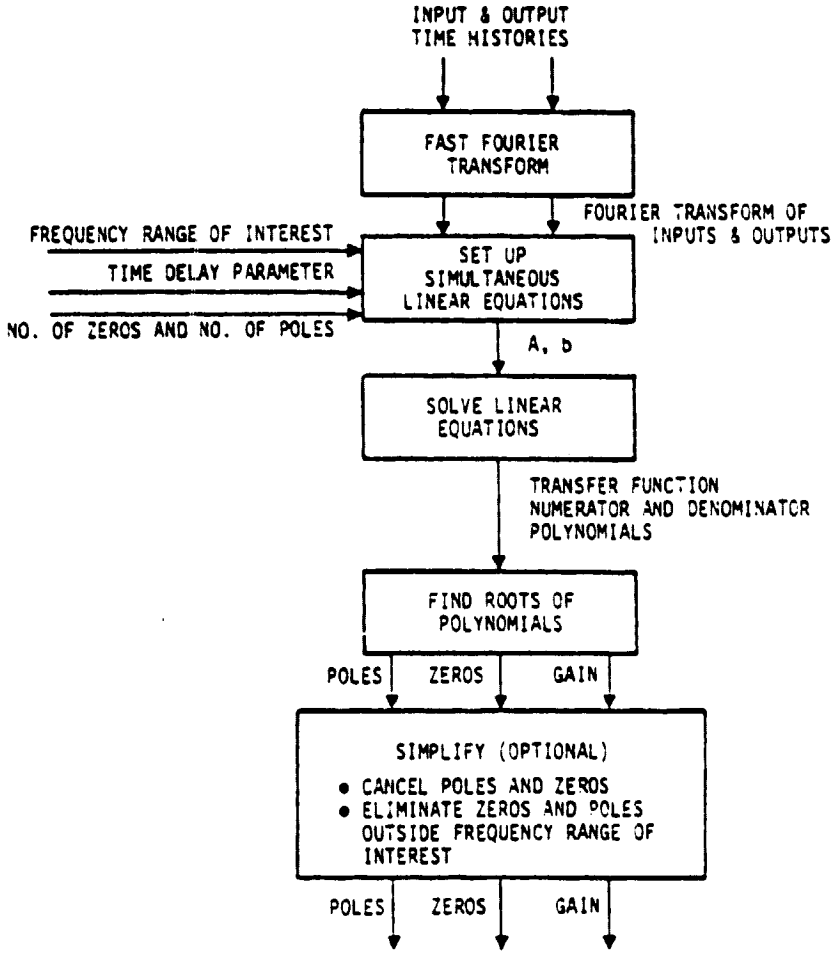

Figure 2.1 Schematic Flowchart of the On-Line Dynamic Modal Estimation Algorithm

III. MODEL ORDER DETERMINATION

In real-time estimation of dynamic stability, the number of important modes is generally not known. Therefore, it is often necessary to estimate the number of significant modes from the input/output measurements. Akaike [16] determines the model order of a system by finding the minimal state-space realization from the associated Hankel matrix. Tse and Weinert [17] find the minimum order by successively increasing the order of a state-space realization until the determinant of the associated prediction of the output covariance shows a sharp drop in magnitude. Rissanen [22] used an entropy argument in a theoretical discussion on model structure identification. Young and Jakeman [23] use the largest eigenvalue and the weighted trace of the parameter error covariance to determine model orders for systems with deterministic inputs. These methods show good results if the disturbances of a system are white. Due to the non-white nature of gust disturbances in aircraft testing it is extremely difficult to estimate the modal order by the above methods.

A fundamentally different approach to the problem of estimating the order of the model based on input/output measurements is proposed here. The basic idea is as follows. If the specified model order is lower than the true model order, the identification algorithm in this chapter will give incorrect estimates of the poles and zeros. If the specified model order is the same as the true model order, correct poles and zeros will be identified. However, if the specified model order is higher than the true model order, there will be many superfluous poles and zeros in addition to the true poles and zeros. The superfluous poles must approximately cancel out the superfluous zeros.

Therefore, if we specify a maximal model order in the algorithm of this chapter, the true model order could be obtained after the transfer function is simplified first by cancelling the poles and zeros which are very close to each other and, secondly, the poles and zeros outside the frequency range of interest.

IV. EXAMPLES OF INSTRUMENTAL VARIABLE MODAL ESTIMATION APPLICATIONS

Instrumental variable modal estimation can be applied to many different model structure and parameter estimation problems. The examples shown in this chapter were chosen for their diversity and availability of data. The flight test data of the B-52, supplied by the Air Force Flight Dynamics Laboratory [AFFDL], are of high quality and are well-suited for dynamic structure identification. The flight test data of the Boeing 747 SCA - Space Shuttle combination include missed data points. The off-shore platform data include no measurements of the inputs and therefore require a significant amount of averaging to reduce biases in the estimates. The space structure data are simulation data with white noise and without any nonlinearities.

4.1 APPLICATION OF THE MODAL ESTIMATION ALGORITHM TO B-52 FLIGHT TEST DATA

Interaction of structural flexibiity with flight modes has been shown to be very important for large and flexible aircraft. The low drag and highly maneuverable design of modern aircraft make them even more flexible and put stringent requirements on the control system design. The control system not only has to provide aircraft stability, but also to control elastic modes to relieve stresses and prevent flutter. These control configured vehicles (CCV) concepts of modern aircraft can only be realized if the aircraft dynamics in general and particularly the aeroelastic behavior is known sufficiently accurately. The AFFDL conducted flight tests with a B-52 CCV specifically designed to provide data for dynamic model and parameter estimation [18].

Accelerometers and gyros were located at different parts of the aircraft (Figure 4.1 and Table 4.1) to measure accelerations

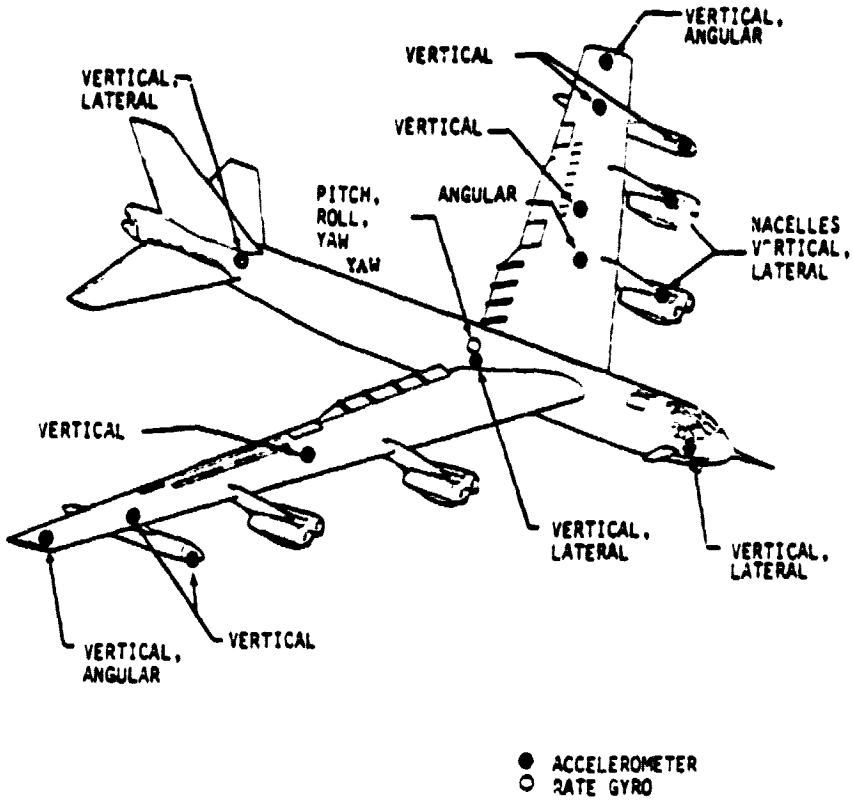

Figure 4.1 Sensor Locations of B-52 CCV

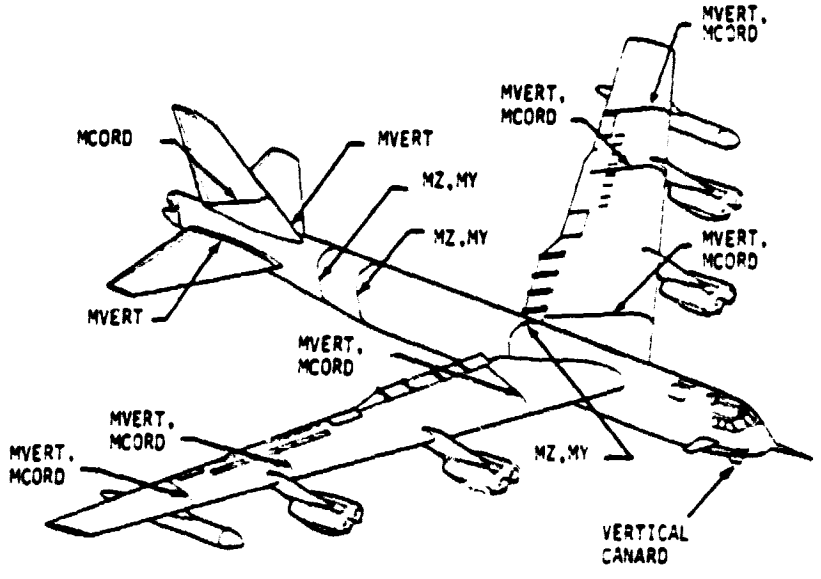

Figure 4.2 Locations of Bending Moment Meaurements on B-52 CCV

Table 4.1
Recorded Flight Test Measurements

NO.	ITEM	LOCATION
1	Vertical Bending Moment	BS760
2	Vertical Bending Moment	BS1222
3	Vertical Bending Moment	BS1412
4	Lateral Bending Moment	BS760
5	Lateral Bending Moment	BS1222
6	Lateral Bending Moment	BS1412
7	Vertical Bending Moment	LWS222
8	Vertical Bending Moment	LWS820
9	Vertical Bending Moment	LWS974
10	Chordwise Bending Moment	LWS222
11	Chordwise Bending Moment	LWS820
12	Chordwise Bending Moment	LWS974
13	Vertical Bending Moment	RWS222
14	Vertical Bending Moment	RWS820
15	Vertical Bending Moment	RWS974
16	Chordwise Bending Moment	RWS222
17	Chordwise Bending Moment	RWS820
18	Chordwise Bending Moment	RWS974
19	Vertical Bending Moment	LHTBL56
20	Vertical Bending Moment	RHTBL56
21	Vertical Bending Moment	FS135
22	Pitch Rate	BS860
23	Roll Rate	BS860
24	Yaw Rate	BS860
25	Vertical Acceleration	BS172
26	Vertical Acceleration	BS860
27	Vertical Acceleration	BS1655
28	Lateral Acceleration	BS172
29	Lateral Acceleration	BS860
30	Lateral Acceleration	BS1655
31	Vertical Acceleration	LWBL565
32	Vertical Acceleration	LWBL925
33	Vertical Acceleration	LWS1359
34	Vertical Acceleration	Left Ext. Tank, Nose
35	Vertical Acceleration	RWBL565
36	Vertical Acceleration	RWBL925
37	Vertical Acceleration	RWS1359
38	Vertical Acceleration	Right Ext. Tank, Nose
39	Vertical Acceleration	Left Inboard Nacelle
40	Lateral Acceleration	Left Inboard Nacelle
41	Vertical Acceleration	Left Outboard Nacelle
42	Lateral Acceleration	Left Outboard Nacelle
43	Angular Acceleration, Y-Axis	LWS540
44	Angular Acceleration, Y-Axis	LWS1359
45	Angular Acceleration, Y-Axis	RWS1359

and angular rates for mode identification; strain gages were attached to measure structural deformations (Figure 4.2 and Table 4.1) to assist in the identification of mode shapes.

For the flight test investigated, the aircraft was flying at an altitude of 21,000 feet at 305 KCAS. The excitation was a vertical cannard sine sweep from 0.5 to 5.0 Hz. Figure 4.3 shows response data of this flight test. In the application of the instrumental variables modal estimation algorithm (IVME) to these data, the frequency range of interest is limited to $0.1 < \omega < 5$ Hz and the number of poles and zeros in each transfer function are specified to be eight and seven, respectively. The minimum time delay for the instrumental variable is,

$$\tau = 2n\Delta t \mid n = \max(\text{poles, zeros}),\ \Delta t = \text{time between measurements}$$

Transfer function measurements with τ, 2τ, and 3τ where combined to improve the estimation accuracy. Discrete frequency noise was eliminated from the data set. Figures 4.4 and 4.5 show the measured transfer functions between te vertical cannard and wing-tip and wing-root, respectively. Elastic modes, as well as aeroelastic modes, are clearly excited in the frequency range of the sine sweep, as observed in the magnitude plots, as well as the phase plots. Table 4.2 compares the theoretical structural modes [18] with the identified frequencies and damping ratios. Some of the identified modes (4, D, 6, G, 9 H) mask the theoretical structural, others (3, C, 7, 8, F) could be low-damped aeroelastic modes.

4.2 APPLICATION OF THE IVME ALGORITHM TO IDENTIFY THE DYNAMICS OF THE BOEING 747 - SPACE SHUTTLE COMBINATION

Boeing has modified the model 747-123 for NASA to carry the Space Shuttle Orbiter aircraft "piggy-back" fashion (Figure 4.6). The dynamics and aerodynamics of this aircraft combination are significantly different from that of the regular B747 and required

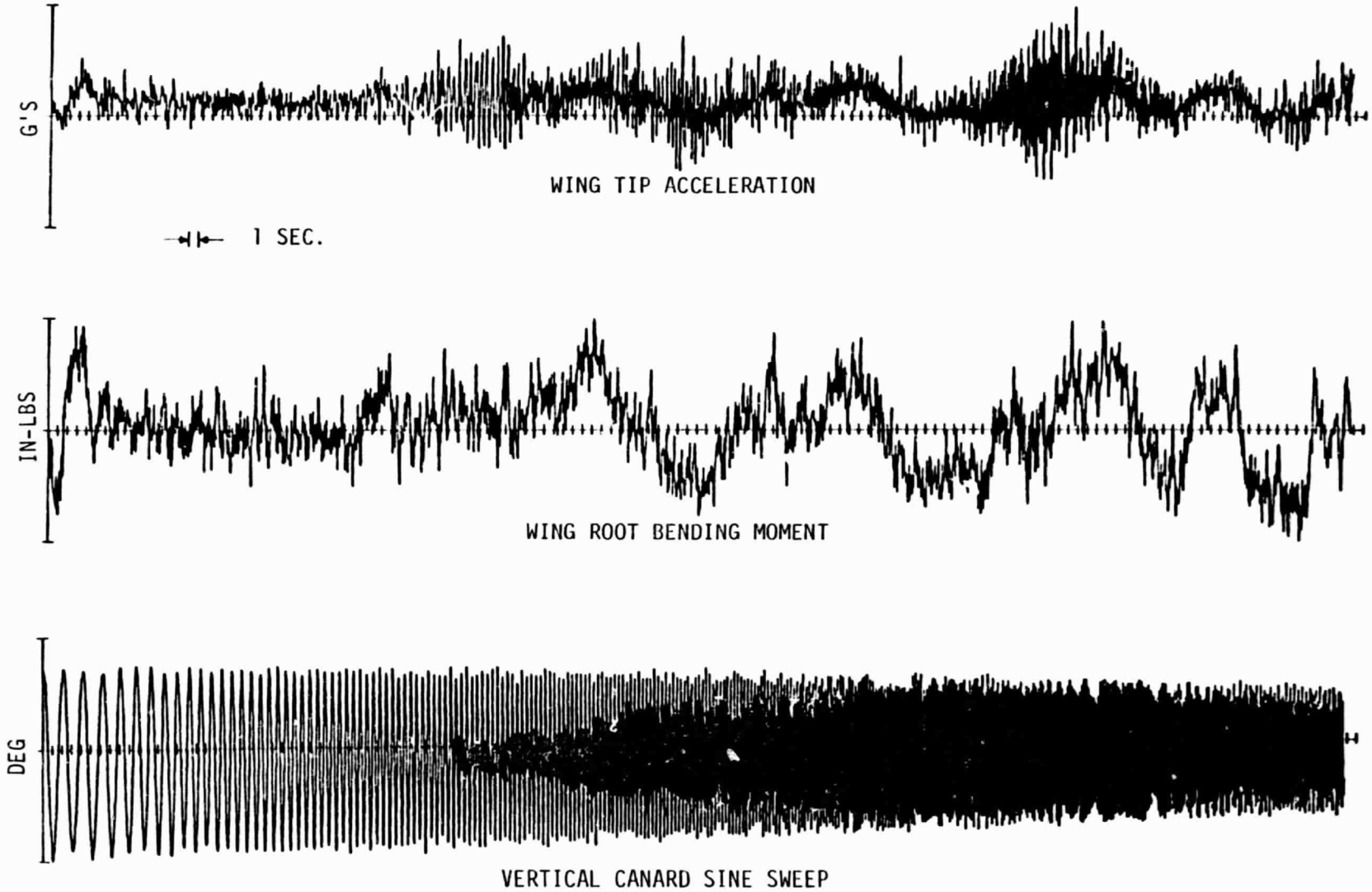

Figure 4.3 Flight Test Response Data

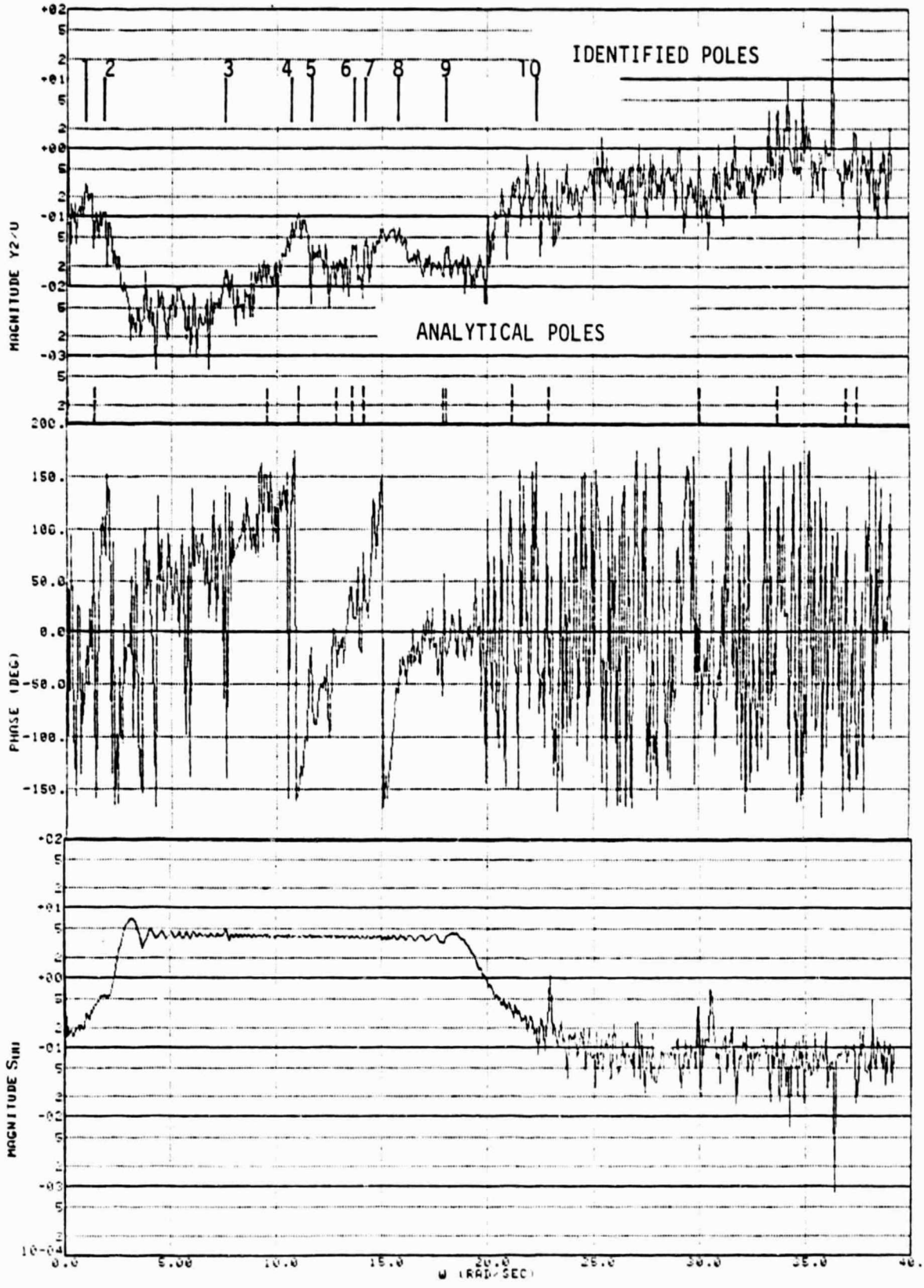

Figure 4.4 B-52 CCV Transfer Function Between Vertical Canard and Wing Tip

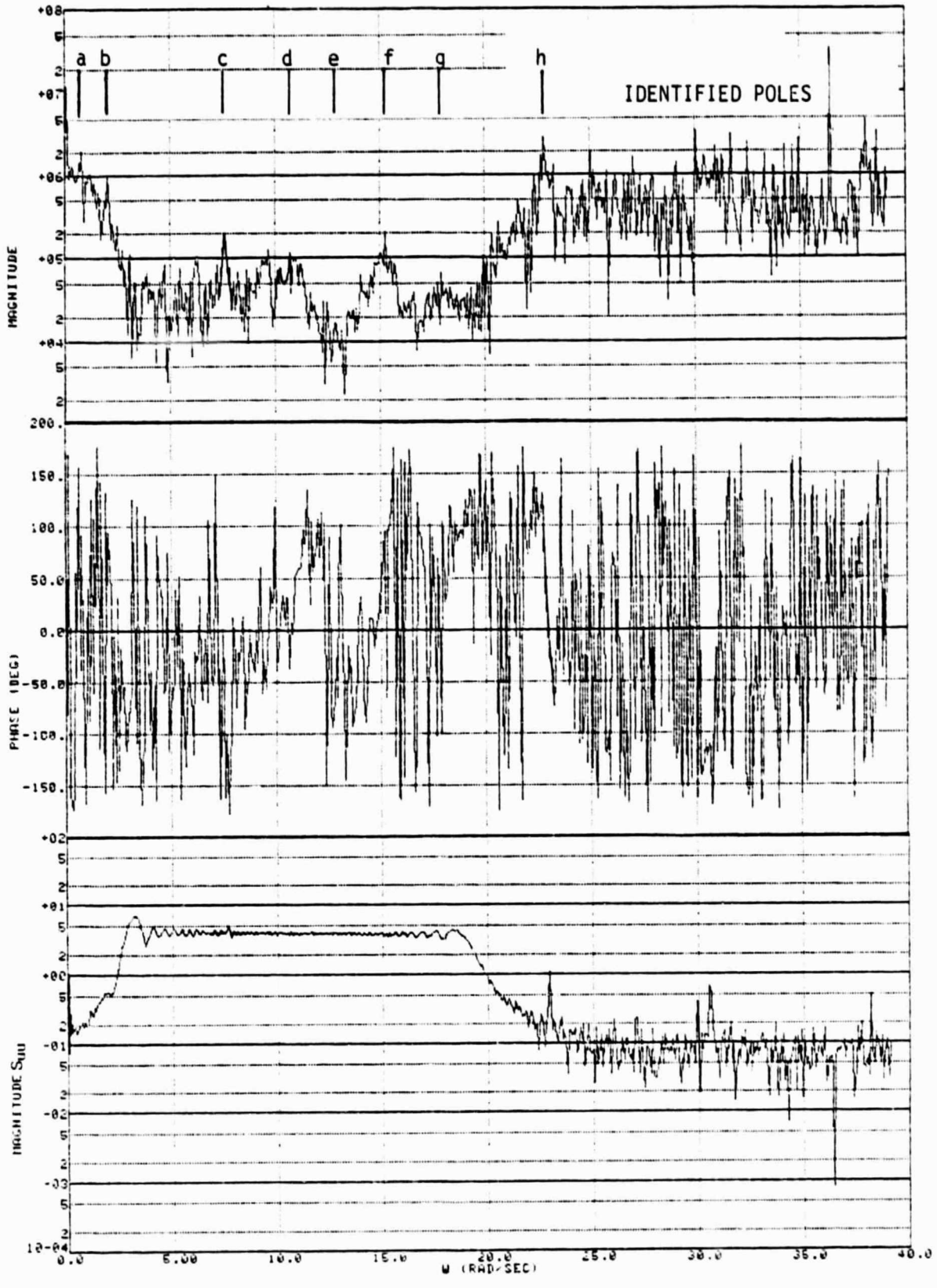

Figure 4.5 B-52 CCV Transfer Function Between Vertical Canard and Wing Root

Table 4.2

Comparison of Theoretical and Identified Modes
(Antisymmetric)

THEORETICAL		WING-TIP ACC		WING BDG MOM	
FREQ (Hz)	DAMP (%)	FREQ (Hz)	DAMP (%)	FREQ (Hz)	DAMP (%)
0.0	100.0	.138[1]	19.0	.135[a]	4.1
.214	8.36	.278[2]	7.4	.351[b]	6.5
		1.258[3]	.9	1.23[c]	1.0
1.159	5.77	1.724[4]	3.9	1.73[d]	7.7
1.761	4.19	1.807[5]	3.9		
2.036	.70	2.165[6]	7.3	2.00[e]	10.4
2.156	10.67				
2.240	1.75	2.337[7]	1.1		
		2.457[8]	1.4	2.45[f]	.6
2.847	1.02				
2.873	17.85	2.88[9]	2.5		
3.372	4.71	3.55[10]	.2		
3.662	3.30			3.64[h]	.6

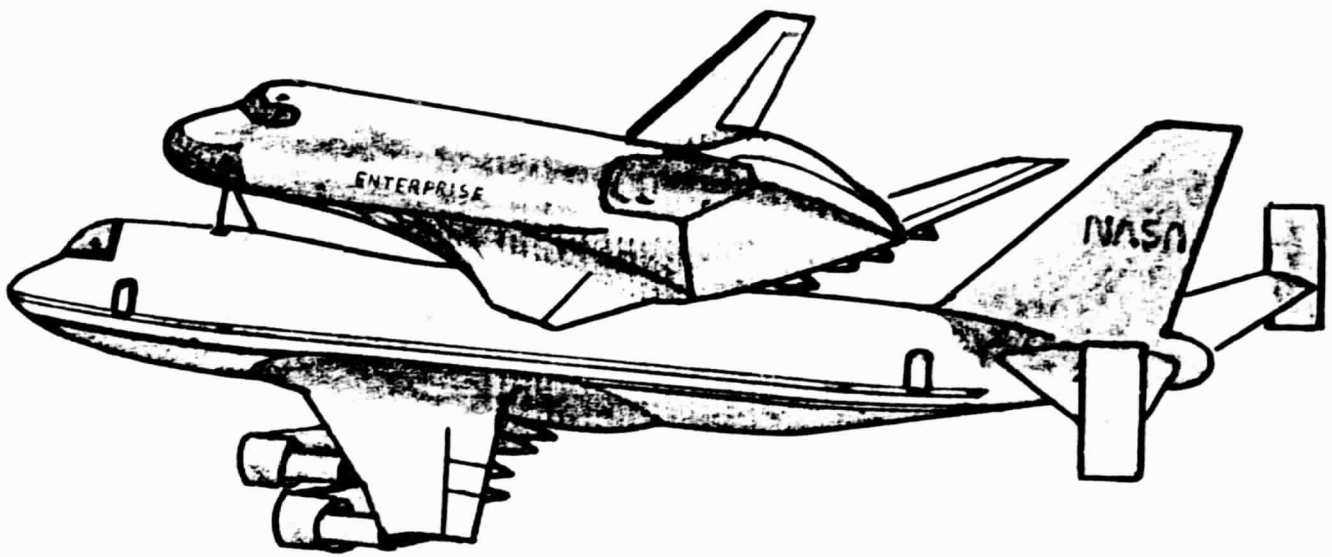

Figure 4.6 Boeing 747 SCA with Space Shuttle Orbiter Enterprise

a new control system design incorporating all the significant modes of the B747-Space Shuttle (B747 SCA). Flight tests were performed by Dryden Flight Research Center to determine the flight envelope of the B747 SCA and to fine tune the control and stability system.

This investigation applies an instrumental variables modal estimation algorithm to flight test data of the B747 SCA to determine its structural and aeroelastic characteristics.

For the flight test investigated, the aircraft was flying at an altitude of 22,000 feet at M = .56. The excitations were rudder and elevator sine sweeps. Figures 4.7 and 4.8 show the power spectra of the rudder and elevator excitations, respectively. These excitations are band-limited and are not constant over the range of excitation frequencies. Table 4.3 shows some of the recorded flight test measurements. For this investigation wing-tip acceleration is used to identify the B747 modes, and the orbiter attachment accelerations to identify the modes of the B747-Space Shuttle combination. Figures 4.9 and 4.10 show the measured transfer functions for the rudder sweep and the elevator sweep, respectively. The measurements show several extremas for missed frequencies during the frequency sweep. Lacking are good measurements for low frequencies, but some modes can be clearly observed. Tables 4.3 and 4.4 show the identified antisymmetric and symmetric modes, respectively. Even so, the measured transfer functions are relatively noisy; the identified modes change only little for different assumptions for poles and zeros of the transfer function. These consistent estimates demonstrate the robustness of instrumental variables estimates, specifically when using multiple correlations for instrumental variables of different time delays.

Table 4.3

Recorded Flight Test Measurements of B747 SCA

NO.	LOCATION	ITEM
1	AINF	Pitch Angle
2	BINF	Side Slip Angle
3	BETAP	Side Slip Angle
4	AR3300A	Pitch Rate CG Flight Test Gyro
5	AR3301A	Roll Rate CG Flight Test Gyro
6	AR3302A	Yaw Rate CG Flight Test Gyro
7	AR0911D	Pitch Angle CG Ins No. 1
8	AH8587D	Roll Angle CG Ins. No. 1
9	AH9533D	Yaw Angle CG Ins Heading, True
10	VTA	True Air Speed
11	QBAR	Barometric Pressure
12	Z	Altitude
13	IH1176A	L Inboard Aileron Pos
14	IH1180A	R Inboard Aileron Pos
15	IH1189A	L Outboard Elev Pos Act
16	IH1192A	L Inboard Elev Pos Act
17	IH1198A	R Inboard Elev Pos Act
18	IH1199A	R Outboard Elev Pos Act
19	IH1207A	Lower Rudder Pos Act
20	IH1211A	Upper Rudder Pos
21	IH1219A	No. 12 Spoiler Pos
22	IH6708A	No. 1 Spoiler Pos
23	AA3360A	Lat CG Accel
24	AA9513A	Normal CG Accel
25	AA3632A	Longitudinal CG Accel
26	AA9514A	Normal Cockpit Accel
27	RA8382A	Lat Cockpit Accel
28	RA1926A	Lat L Aft Orb Attach Ftng Acce
29	RA1927A	Longitudinal Fwd Orb Attch Ftn
30	RA1956A	Normal Fwd Orb Up Atch Ftng Ac
31	RA1957A	Lat Fwd Orb Attach Ftng Accel
32	RA1958A	Normal L Aft Orb Up Atch Ftng
33	RA1961A	Normal R Aft Orb Up Atch Ftng
34	RA2567A	Lat L Tip Fin Lower FS Accel
35	RA2568A	Lat L Tip Fin Upper FS Accel
36	RA2593A	Lat R Tip Fin Upper FS Accel
37	RA4506A	Normal Aft Fus BS 2300 Accel
38	RA6149A	Lat Tip Vert Tail FS Accel
39	RA6151A	Lat Tip Vert Tail RS Accel
40	RA6224A	Lat Eng 1 Forward Accel
41	RA6225A	Lat Eng 2 Forward Accel
42	RA6324A	Normal Eng 1 Fwd Accel
43	RA6325A	Normal Eng 2 Fwd Accel
44	RA6375A	Normal R Horiz Tail FS Accel
45	RA6377A	Normal R Horiz Tail RS Accel
46	RA6379A	Normal L Horiz Tail FS Accel
47	RA6381A	Normal L Horiz Tail RS Accel
48	RG6384A	Lat Stab Jack Screw Accel
49	RG6386A	Long L Stab Tip Accel
50	RA6392A	Normal R Wing Tip RS Accel
51	RA6389A	Normal L Wing Tip RS Accel
52	RA6393A	Normal L Wing Tip FS Accel
53	RA9442A	Lat Aft Fus BS 2300 Accel
54	XX2569	LH Tip Fin LWR Long Acc
55	XX2570	LH Tip Fin Upr Long Acc
56	XX3361	Normal Accel
57	IH 53A	L Outboard Aileron Pos at Act
58	IH1181A	R Outboard Aileron Pos
59	IH6711A	No. 3 Spoiler Pos
60	IH6705A	No. 5 Spoiler Pos
61	IH7293A	No. 8 Spoiler Pos
62	IH1218A	No. 10 Spoiler Pos

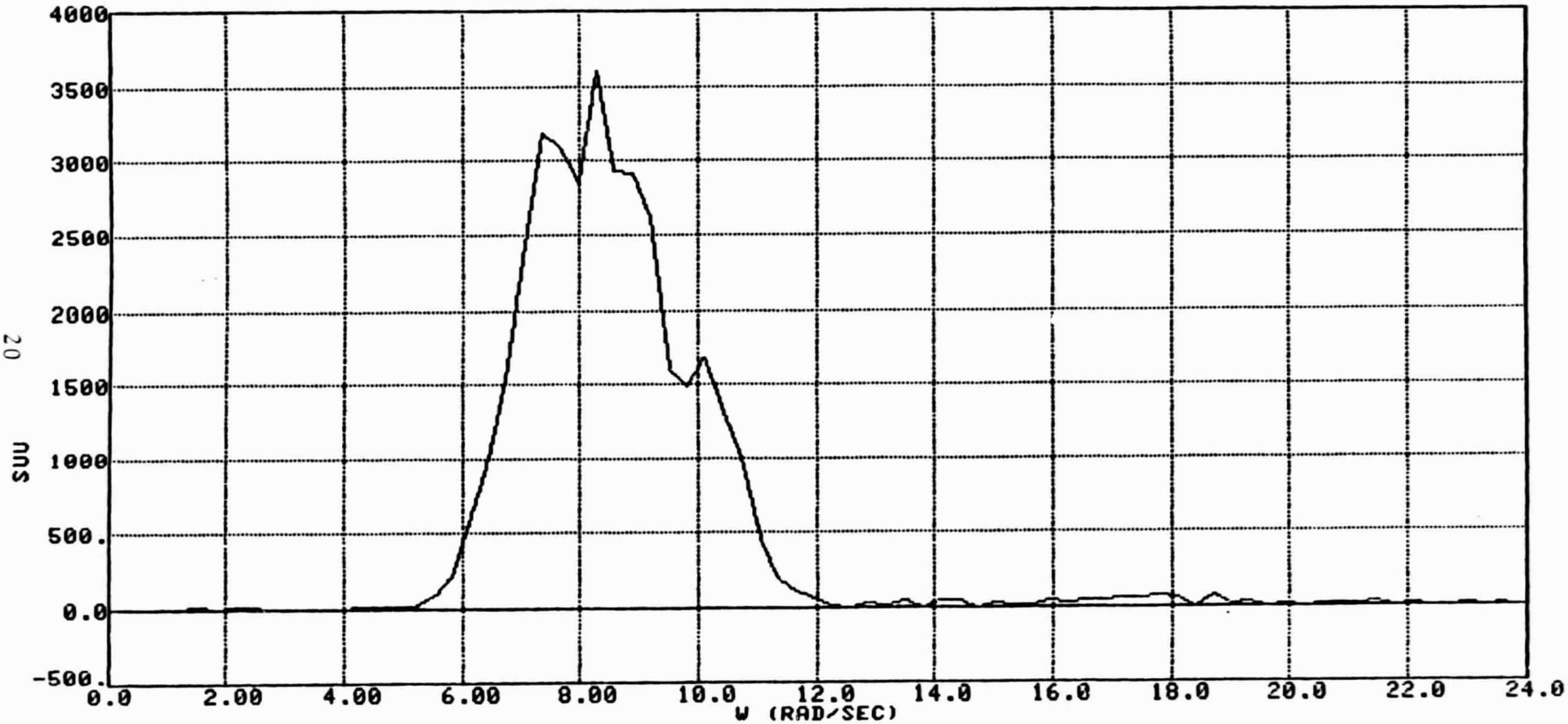

Figure 4.7 Power Spectrum of Lower Rudder Position of B747 SCA
(Flight 01-25-77, 12:28:47 – 12:29:22, $\Delta t = 0.1$ sec)

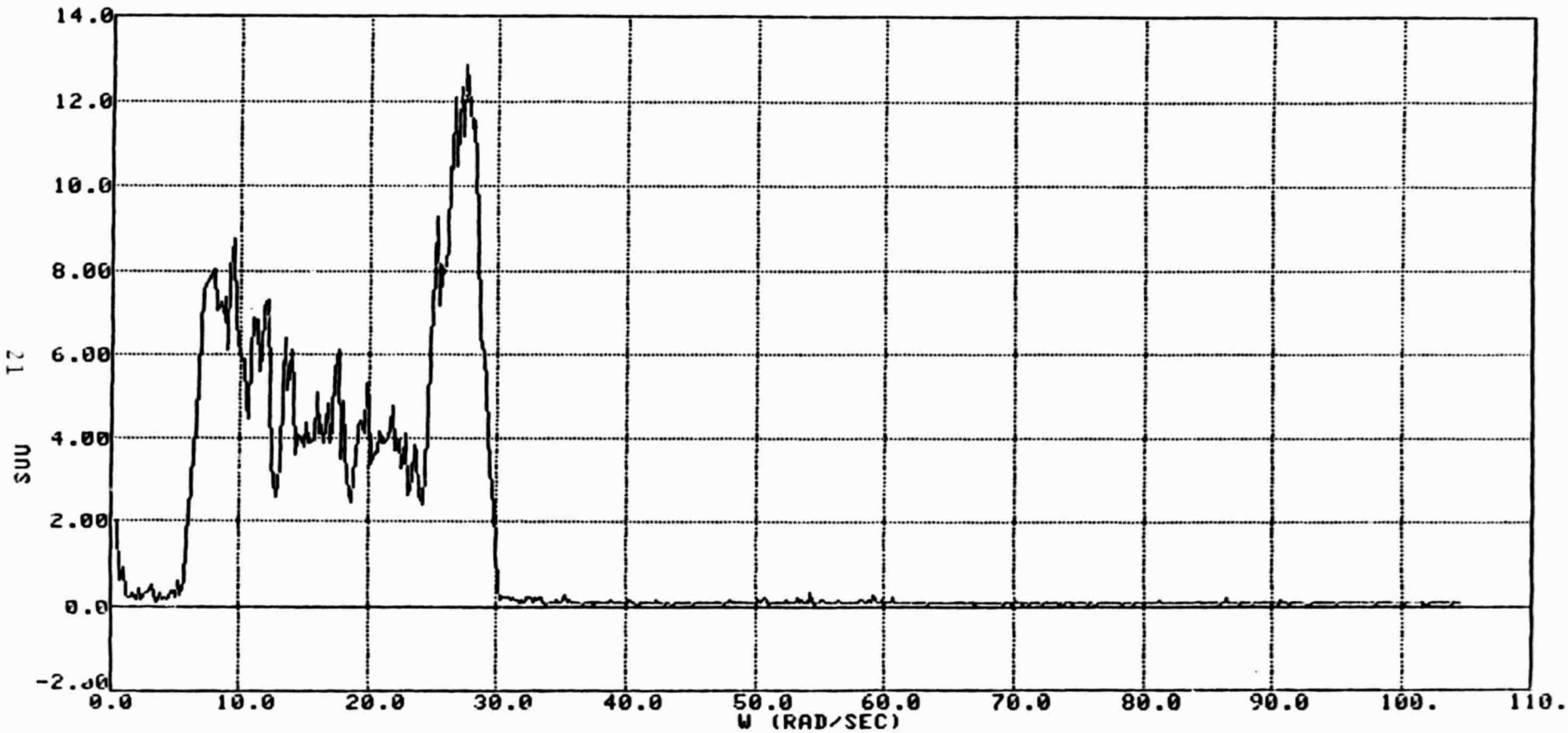

Figure 4.8 Power Spectrum of Right In-Board Elevator Position of B747 SCA
(Flight 01-25-77, 12:31:36 – 12:33:11, Δt = 0.1 sec)

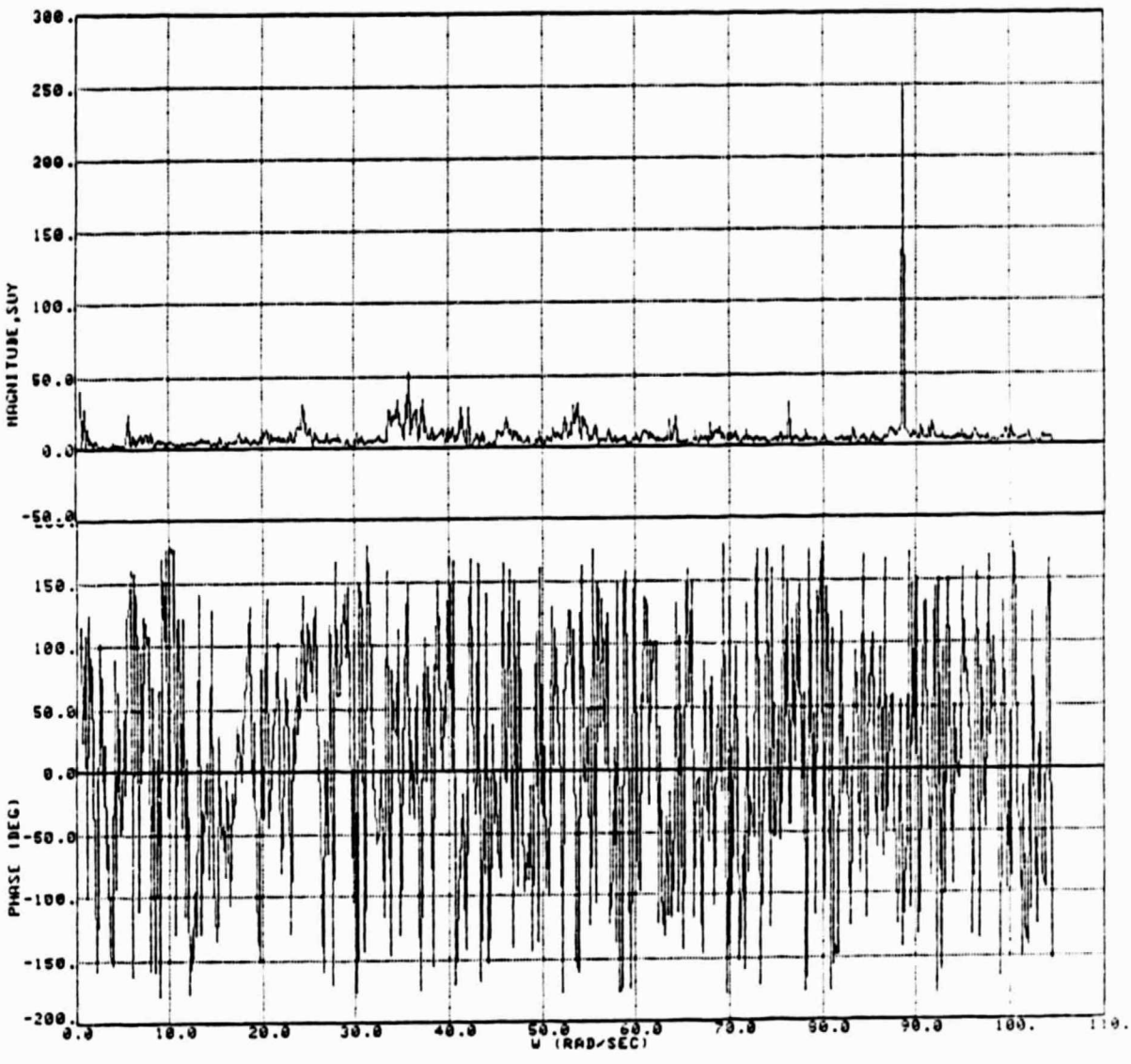

Figure 4.9a Measured Transfer Function of B747 SCA Between Lower Rudder and Lateral Forward Orbiter Attachment Fitting Acceleration (R-Sweep 01-25-77, 1024 Points/Record)

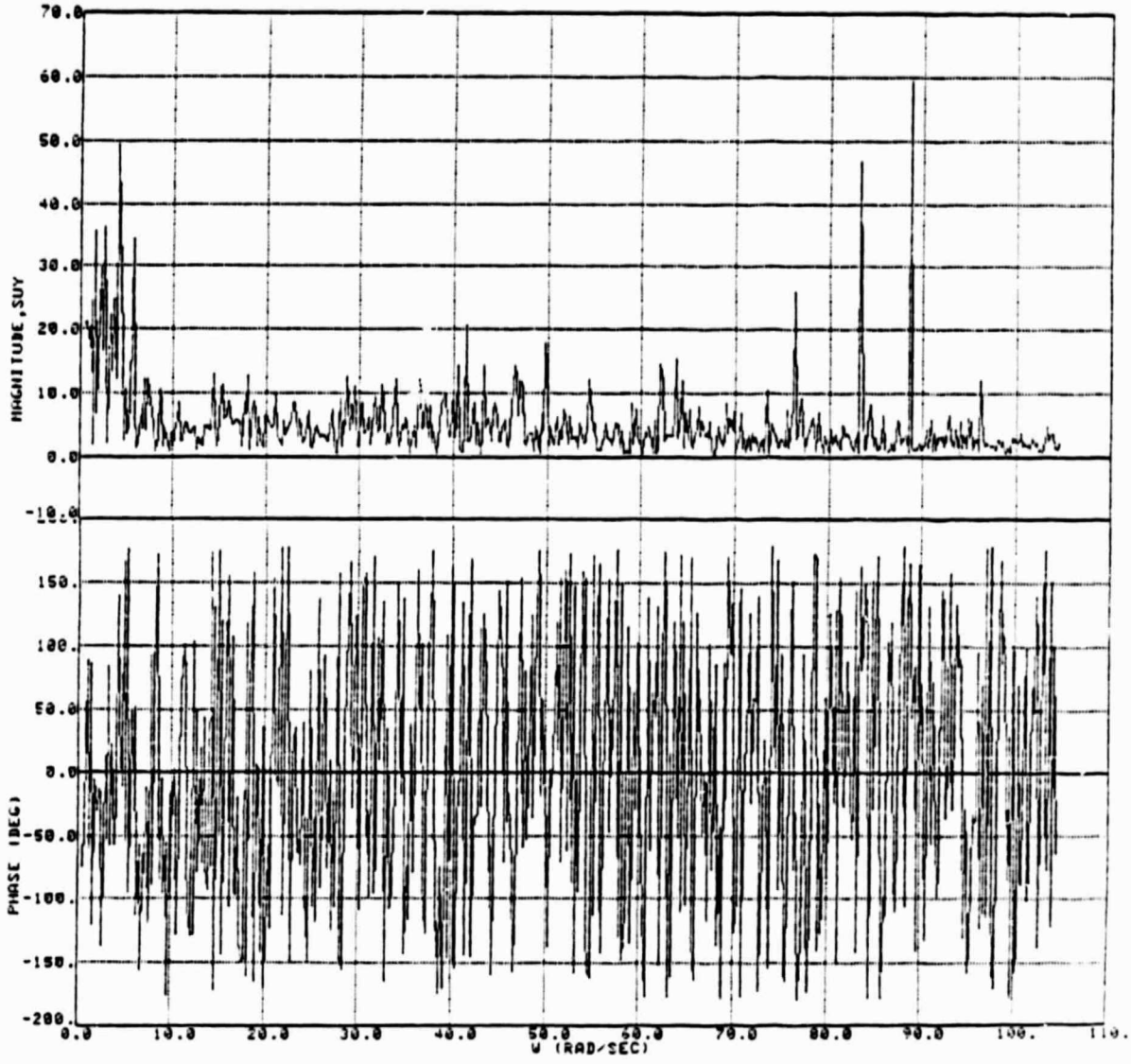

Figure 4.9b Measured Transfer Function of B747 SCA Between Lower Rudder and Differences of Normal Accelerations of Left and Right Aft Upper Orbiter Attachment Fittings (R-Sweep 01-25-77, 1024 Points/Record, Three Averages)

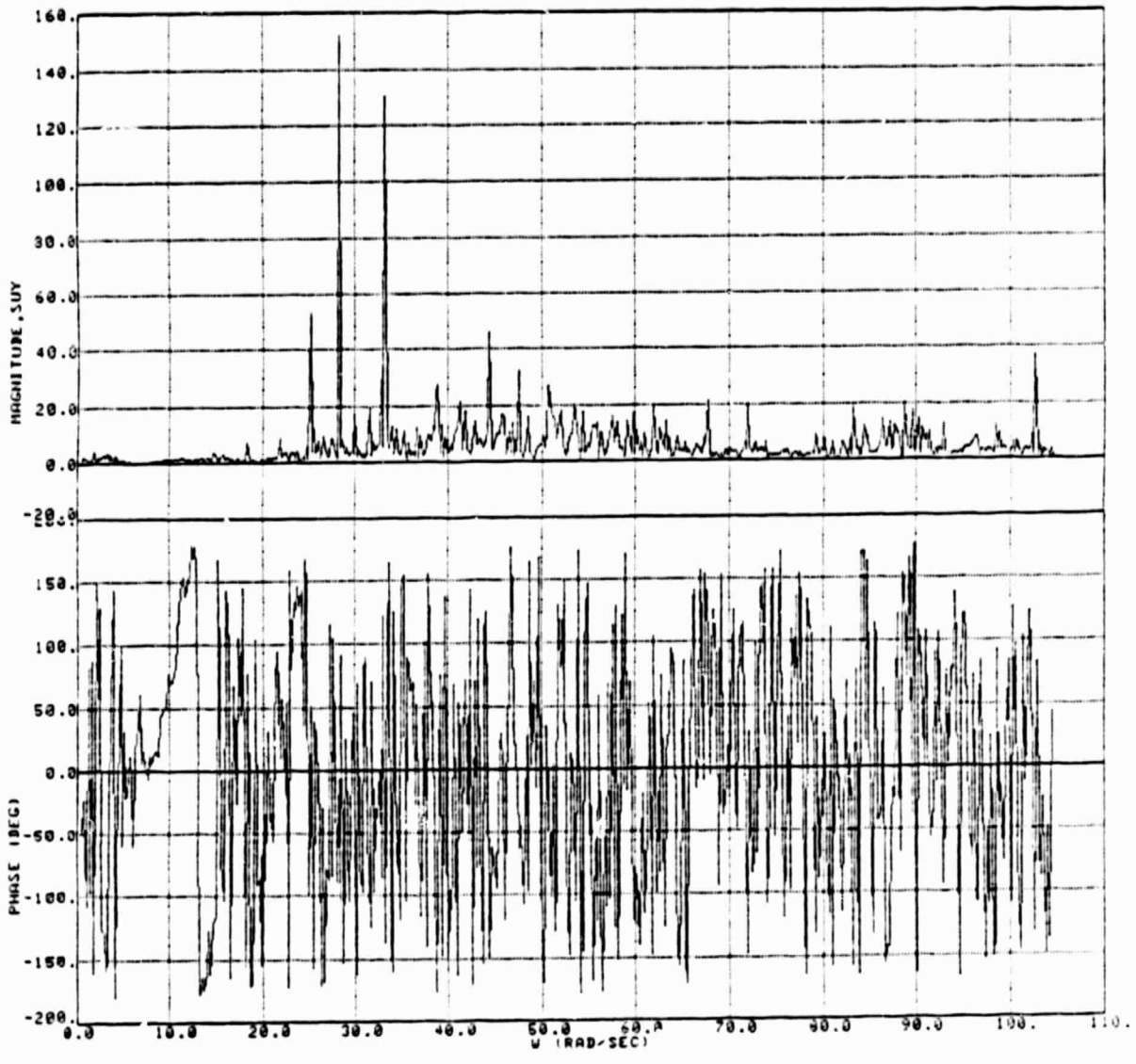

Figure 4.9c Measured Transfer Function of B747 SCA Between Lower Rudder and Differences of Wing-Tip Accelerations (R-Sweep 01-25-77, 1024 Points/Record, Three Averages)

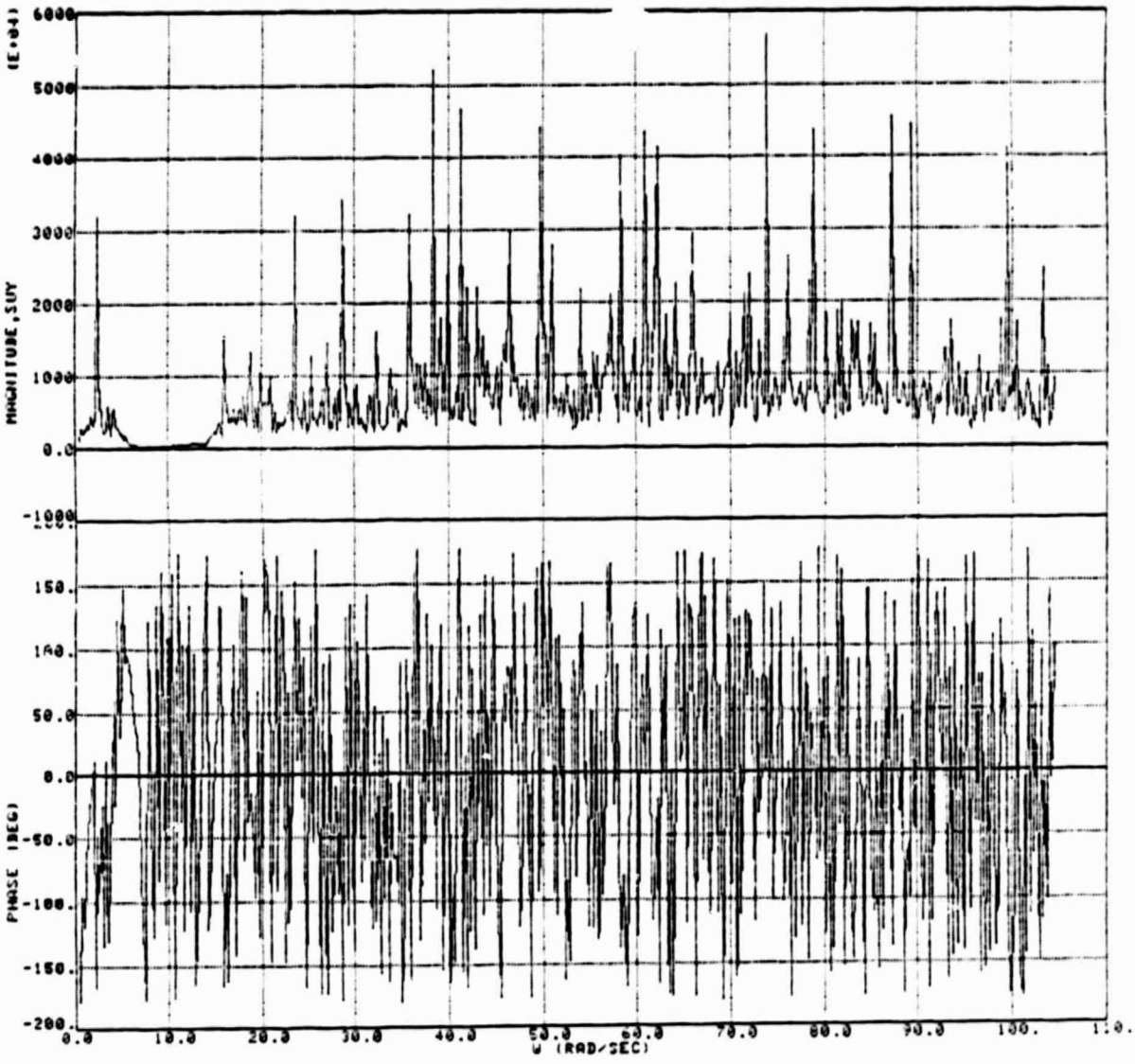

Figure 4.10a Measured Transfer Function of B747 SCA Between Inner Elevator and Normal Forward Orbiter Attachment Fitting Acceleration (E-Sweep 01-25-77, 1024 Points/Record, 12 Averages)

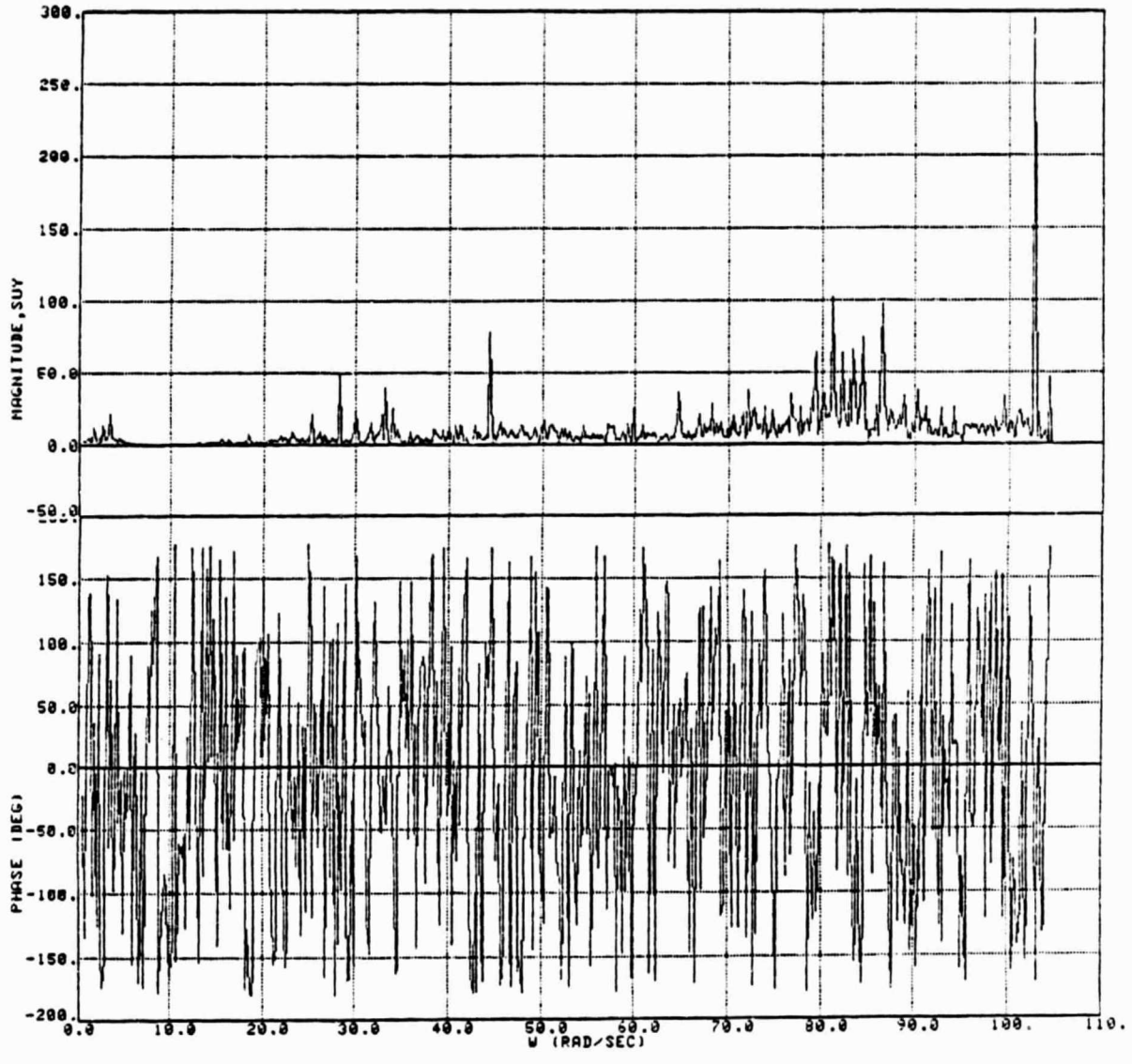

Figure 4.10b Measured Transfer Function of B747 SCA Between Elevator and c.g. Pitch Rate (E-Sweep 01-25-77, 1024 Points/Record, 12 Averages)

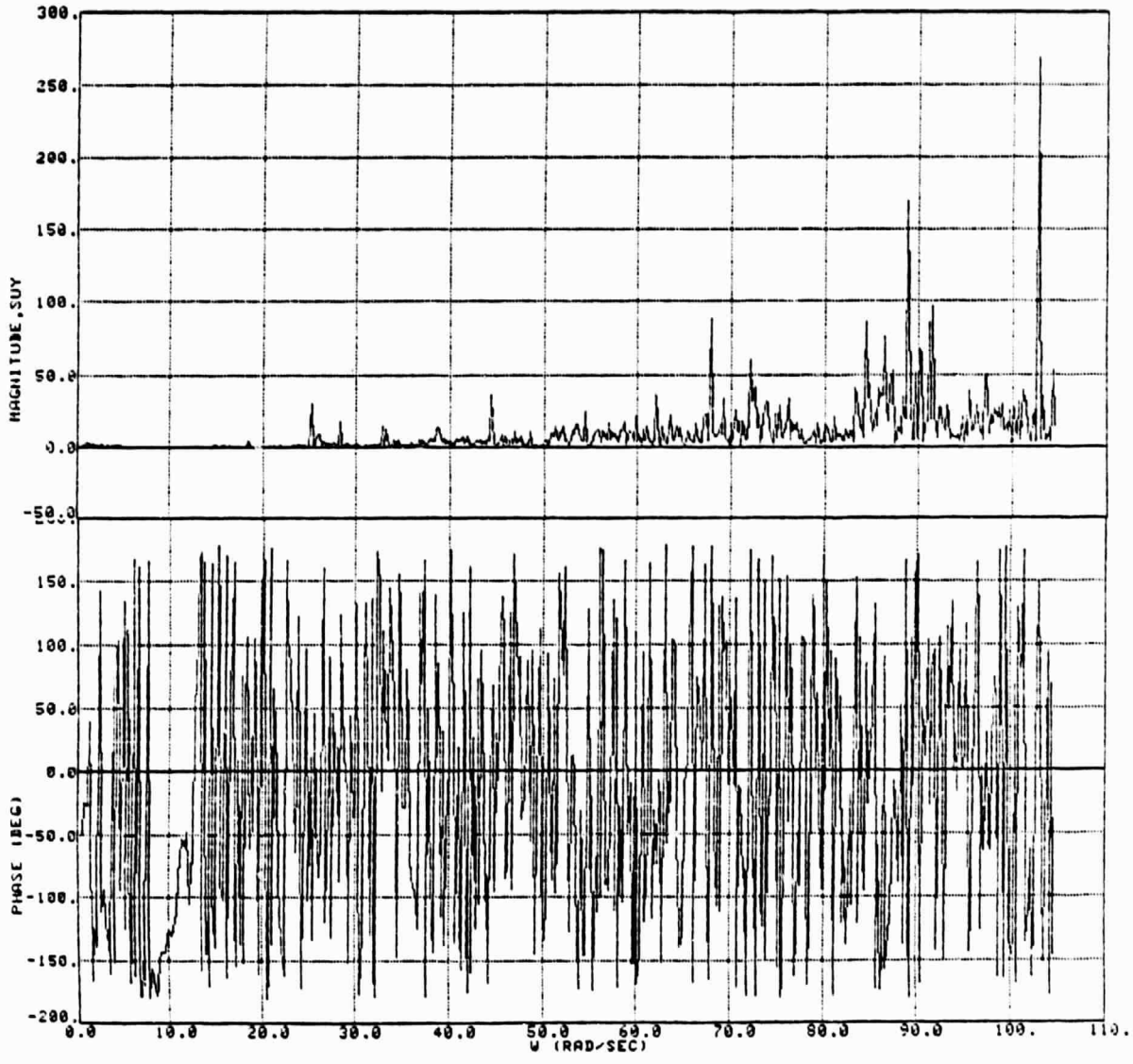

Figure 4.10c Measured Transfer Function of B747 SCA Between Inner Elevator and Sum of Wing-Tip Accelerations (E-Sweep 01-25-77, 1024 Points/ Record, 12 Averages)

Table 4.4

Identified Antisymmetric Modes of the B747 SCA
(R-Sweep 01-25-77, 1024 Points/Record)

NP	NZ	FREQ (Hz)	DAMP (%)	COMMENT
8	7	4.03	1.5	AFT ORB ATT
8	7	13.02	1.6	AFT ORB ATT
8	7	1.81	15.4	LAT FWD ORB ATT
8	7	4.02	.1	LAT FWD ORB ATT
8	7	11.50	.3	LAT FWD ORB ATT
4	7	13.06	3.9	LAT FWD ORB ATT
8	3	.47	1.6	L-R WING TIP ACC
8	3	.82	8.6	L-R WING TIP ACC
8	5	2.55	2.5	L-R WING TIP ACC
8	7	3.65	3.8	L-R WING TIP ACC
8	7	7.23	5.2	L-R WING TIP ACC
8	7	8.08	1.3	L-R WING TIP ACC
8	7	9.42	1.1	L-R WING TIP ACC
8	7	16.33	.2	L-R WING TIP ACC

Table 4.5

Identified Symmetric Modes of the B747 SCA
(E-Sweep 01-25-77, 1024 Points/Record)

NP	NZ	FREQ (Hz)	DAMP (%)	COMMENT
8	3	.43	11.0	WING TIP ACC
8	7	.43	10.9	WING TIP ACC
8	1	1.00	2.2	WING TIP ACC
8	7	1.00	2.1	WING TIP ACC
8	3	4.03	4.6	WING TIP ACC
8	7	4.02	4.6	WING TIP ACC
8	3	8.67	3.3	WING TIP ACC
8	7	8.66	3.2	WING TIP ACC
8	3	10.58	4.4	WING TIP ACC

4.3 APPLICATION OF THE IVME ALGORITHM TO OFF-SHORE PLATFORM DATA

The accident of the oil platform off the coast of Norway this year shows the importance of having a good understanding of the dynamics of off-shore platforms and its interaction with the ocean environment. It is of particular interest to know the structural modes and damping characteristics of the platforms. Measuring and identifying these eigenmodes will assist in determining the safety of new platforms at different sea states and points towards the need for additional passive or active damping of existing platforms.

In Ref. 8, J.K. VanDiver and R.B. Campbell used maximum entropic spectral analysis to identify structural modes of off-shore platforms from accelerometer measurements as shown in Figure 4.11. The instrumental variables modal estimation algorithm is applied here to the same data used in Ref. 8. The input to the structure is assumed to be random noise. The zero-input variation (A-7) of the algorithm therefore is used for this problem in mode identification. Since no phase information is available from these data, the accuracy of the mode estimates is much reduced and many data sets have to be averaged to achieve sufficient certainty in the estimated eigen-frequencies and damping factors of the structures.

The resolution of data in the frequency domain increases with the observation time. The maximum frequency is proportional to the sample rate. The accuracy of mode estimates at low frequencies therefore can be improved by increasing the number of independent data sets, to be averaged, by jumping over data points. If the sample rate is $r = 1/\Delta t$, but the maximum frequency of interest is ω_{max},

$$n_s = \text{integer } (\frac{\omega_{max}}{2r})$$

data sets can be averaged. For high-order systems it is necessary to run the data sets though a band limited filter to avoid alienation due to higher frequencies.

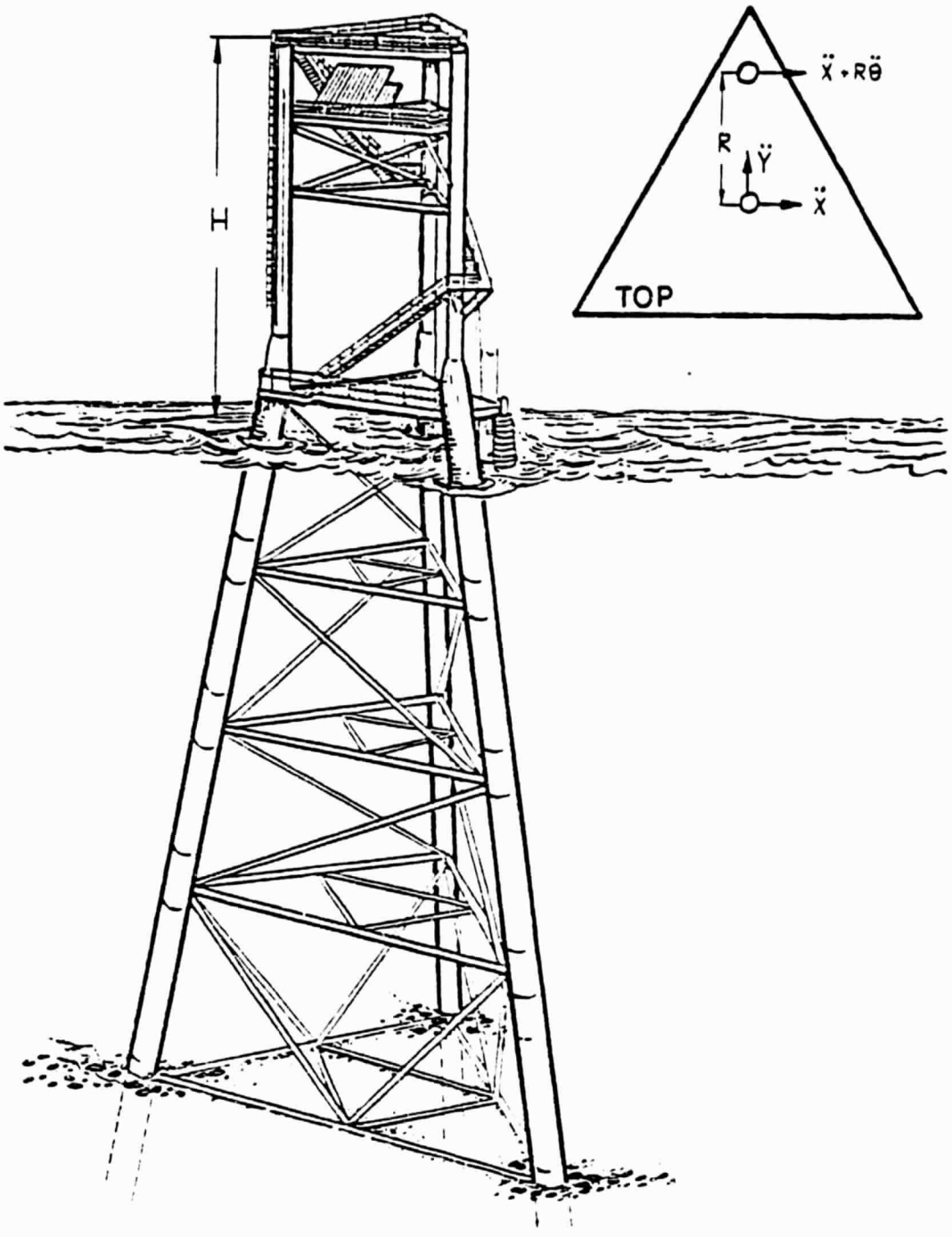

Figure 4.11 Off-Shore Platform [8]

Figures 4.12 and 4.13 show the spectra for 2048 data/record, 28 records averaged and 1024 data/record, 44 records averaged, respectively. The spectra in Figure 4.12 have a higher resolution than the spectra of Figure 4.13. They are, on the other hand, more noisy and give a larger variance in the damping-ratio estimates. Table 4.6 compares the estimated eigen-frequencies and damping ratios of the off-shore platform with the results of VanDiver/Campbell [8] and the theoretical values [8]. The estimated modes determined by IVME are similar to the estimates determined by the MEM [8,10]. Both of these estimates are significantly different from the theoretical modes of the elastic model structure of the platform. This clearly shows the necessity of identifying eigen-frequencies and damping ratios of installed platforms to determine the safety of the platform at different sea states as well as the requirement for passive and/or active damping elements.

4.4 APPLICATION OF THE IVME ALGORITHM TO SPACE-STRUCTURE MODAL ESTIMATION

In the past, the flexibility of spacecraft had a minor impact on the mission performance. Analysis was largely confined to load analysis during launch and the structural interaction with the attitude controller. The spacecraft could, in principle, be treated as rigid with flexibility in the appendages. Techniques for stabilizing the attitude usually relied on frequency separation, where the lowest mode was kept separated from the control bandwidth. Large space structures (LSS) will be erected in space, free of the constraints on configuration imposed by the launch environment. Spacecraft no longer retain the central rigid body, but require distributed structural flexibility. LSS have more similarities with a large leaf of thin paper than the classical point-mass model of previous spacecraft. Closed-loop controllers, which apply forces to the structure based on sensed

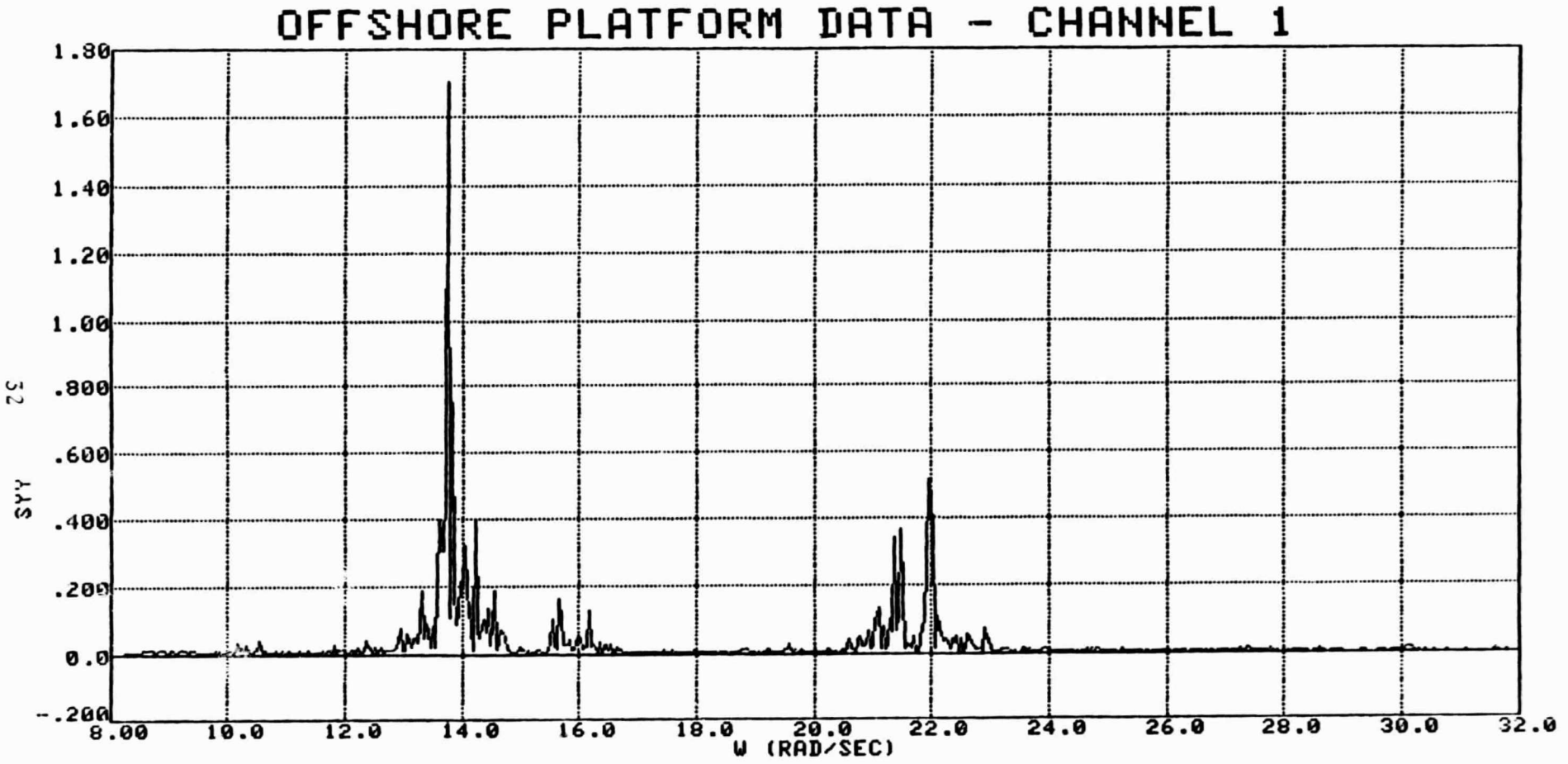

Figure 4.12a Spectrum of Acceleration in x Direction; Number of Data Points per Record (MDP) = 2048; Number of Averages = 28; Number of Shifted Records = 4

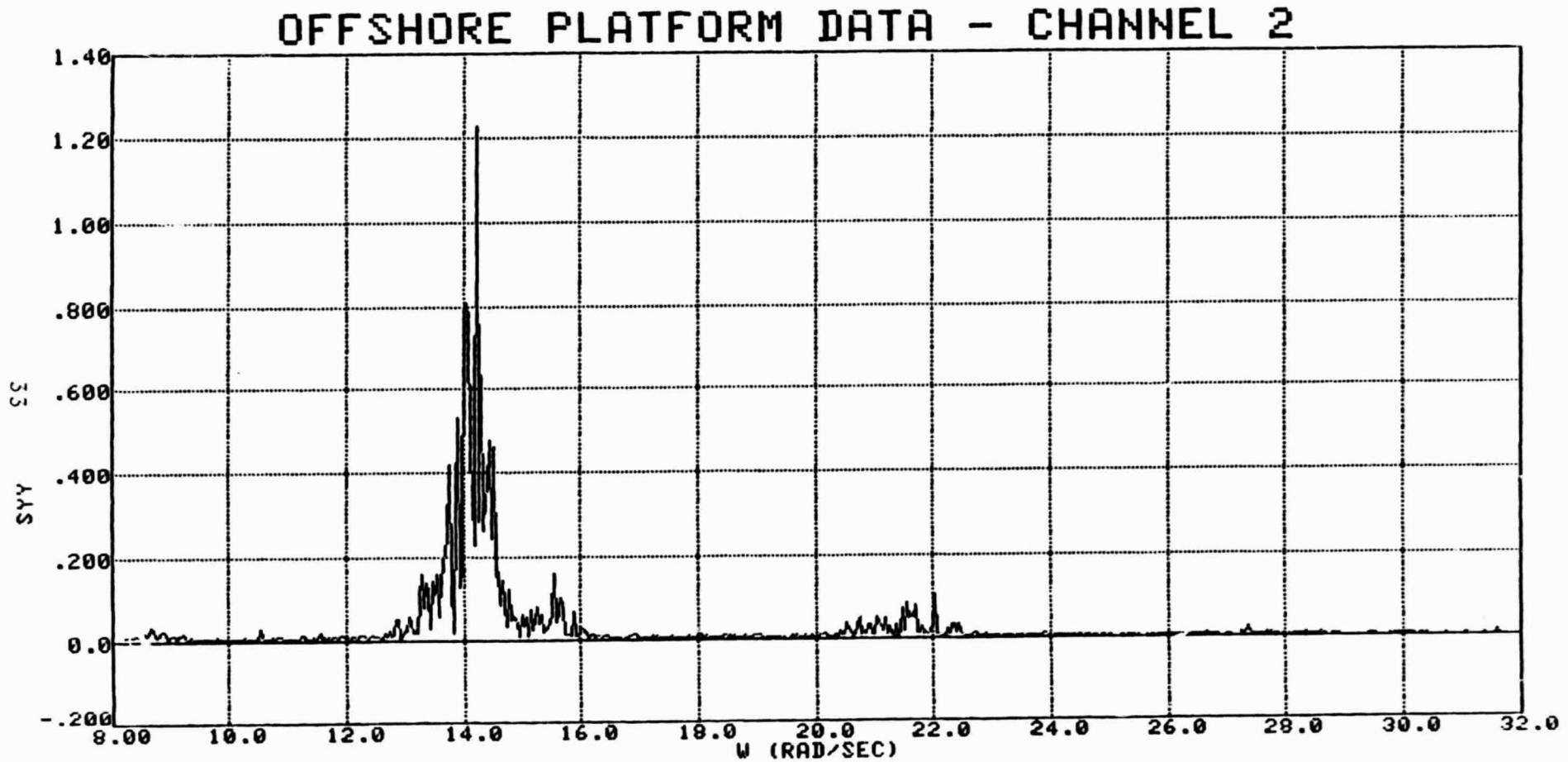

Figure 4.12b Spectrum of Acceleration in y Direction

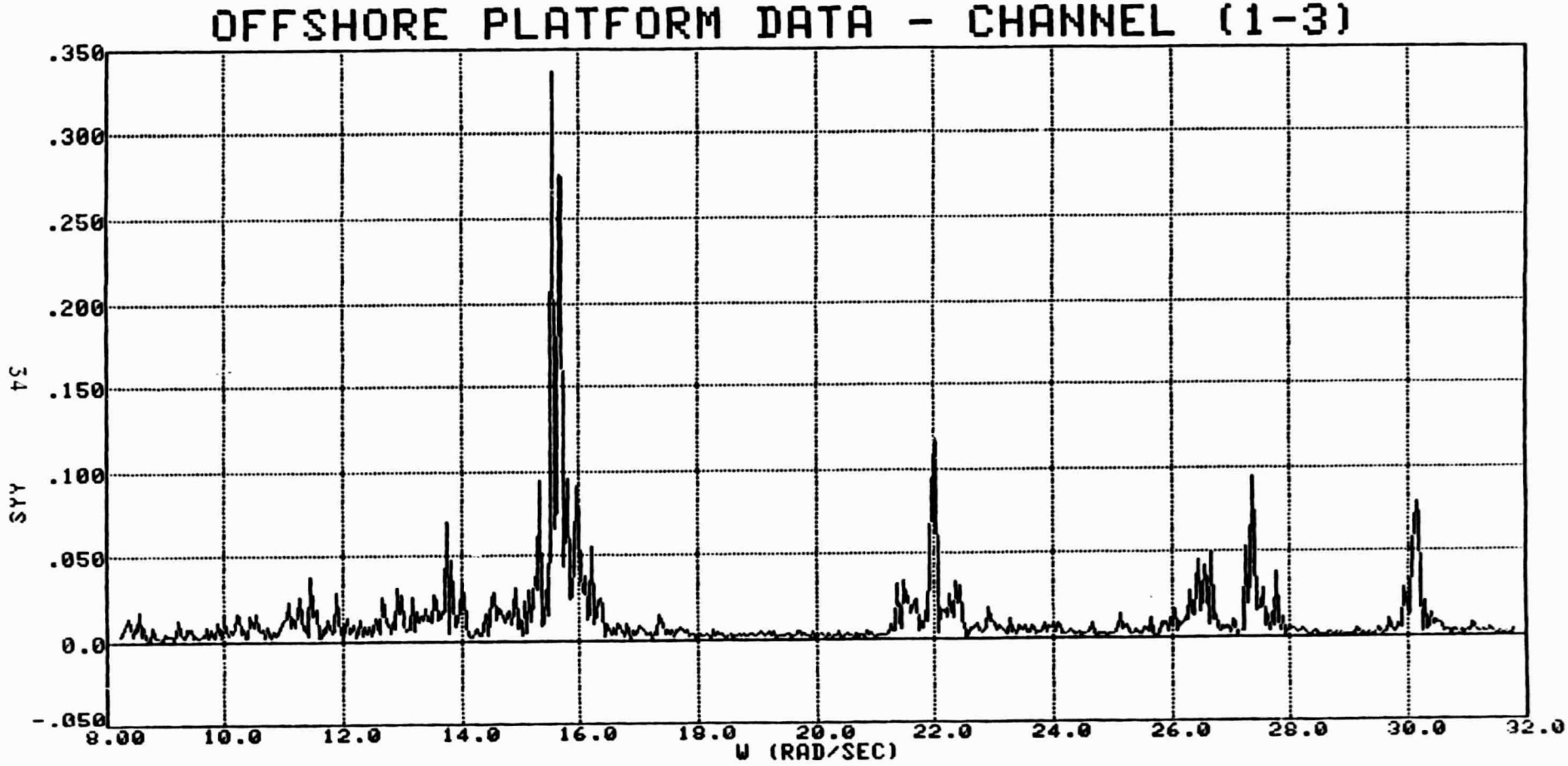

Figure 4.12c Spectrum of Rotational Acceleration

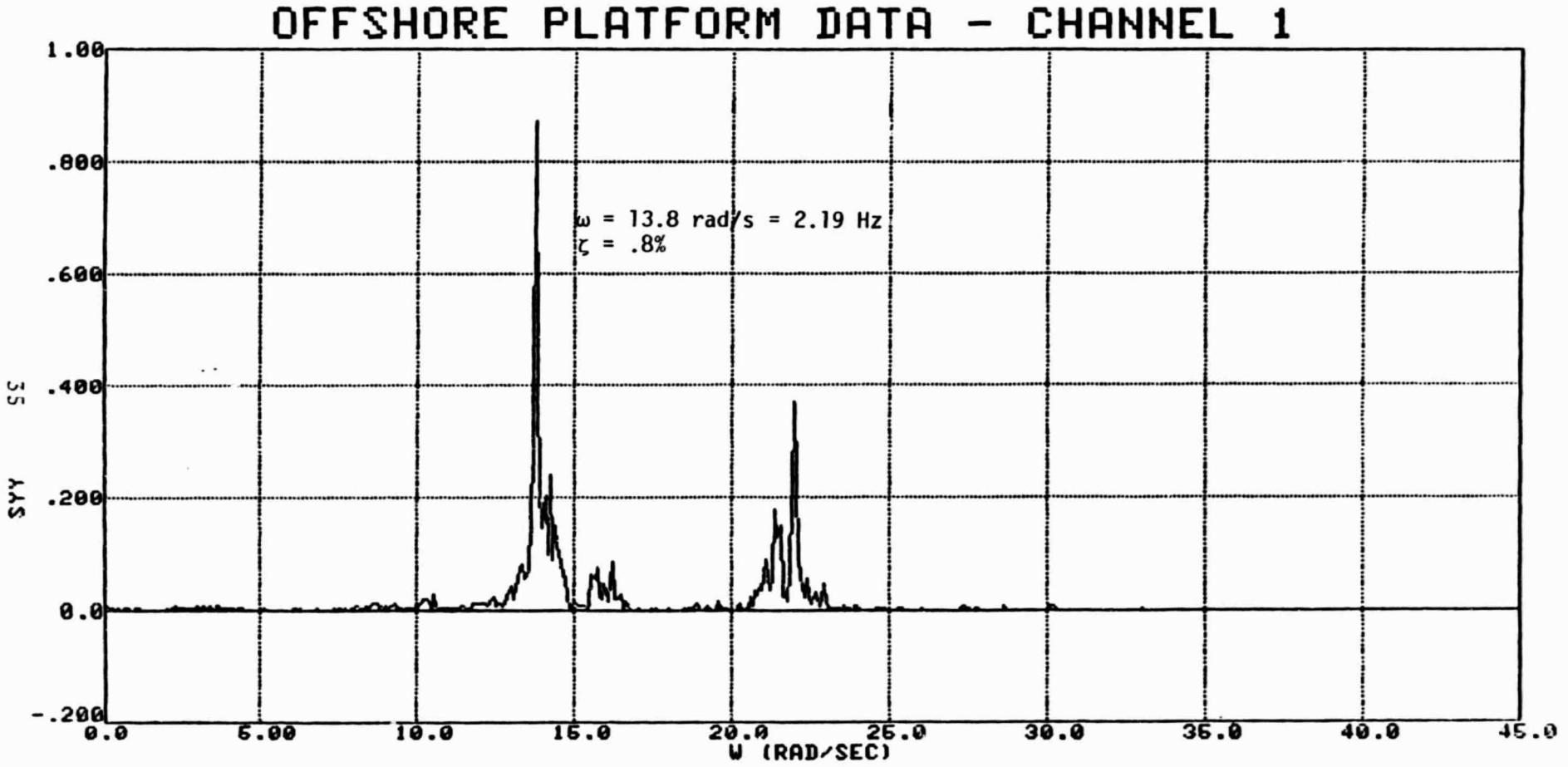

Figure 4.13a Spectrum of Acceleration in x Direction; Number of Data Points per Record = 1024; Number of Averages - 114; Number of Shifted Records = 4

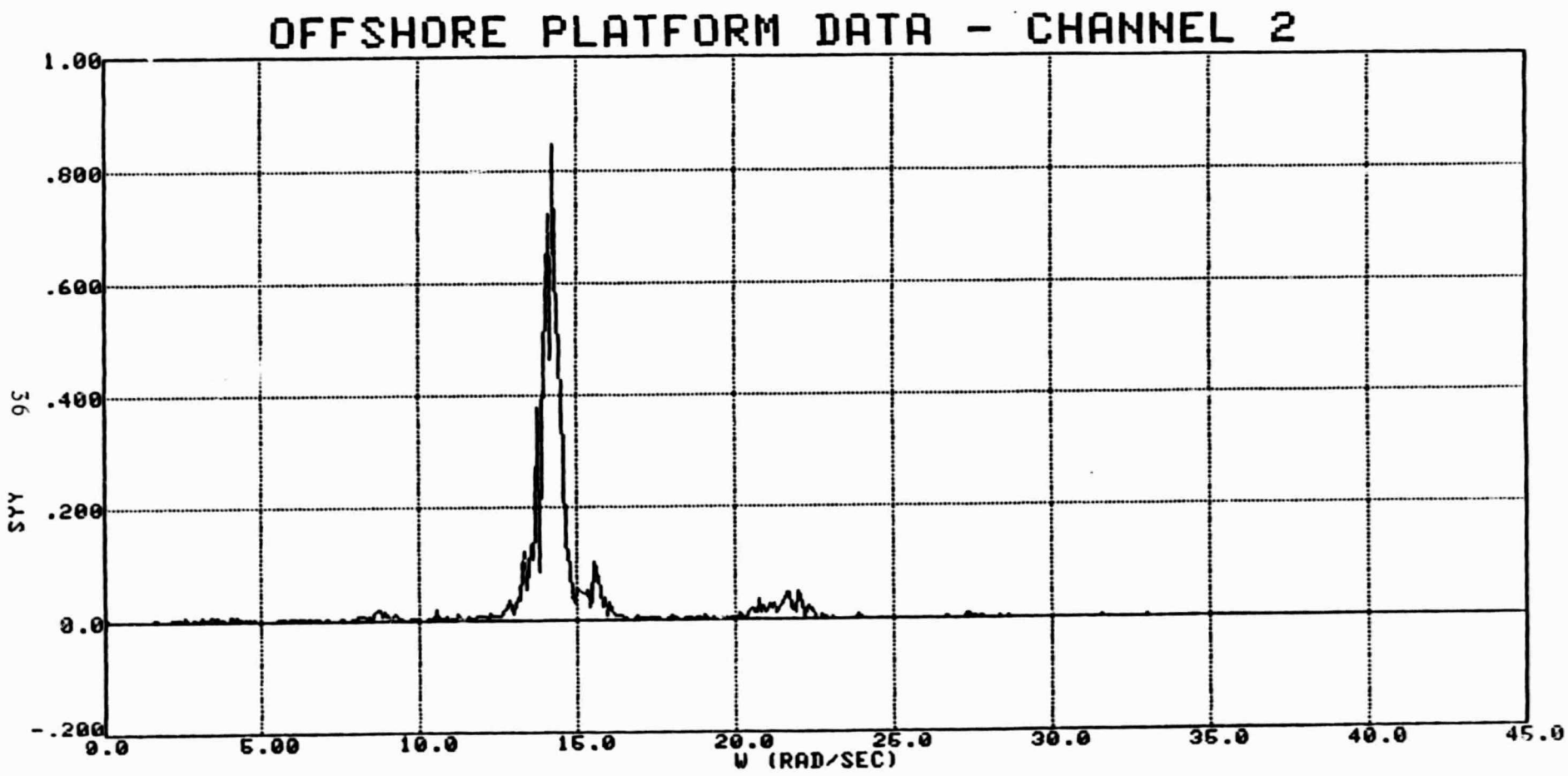

Figure 4.13b Spectrum of Acceleration in y Direction

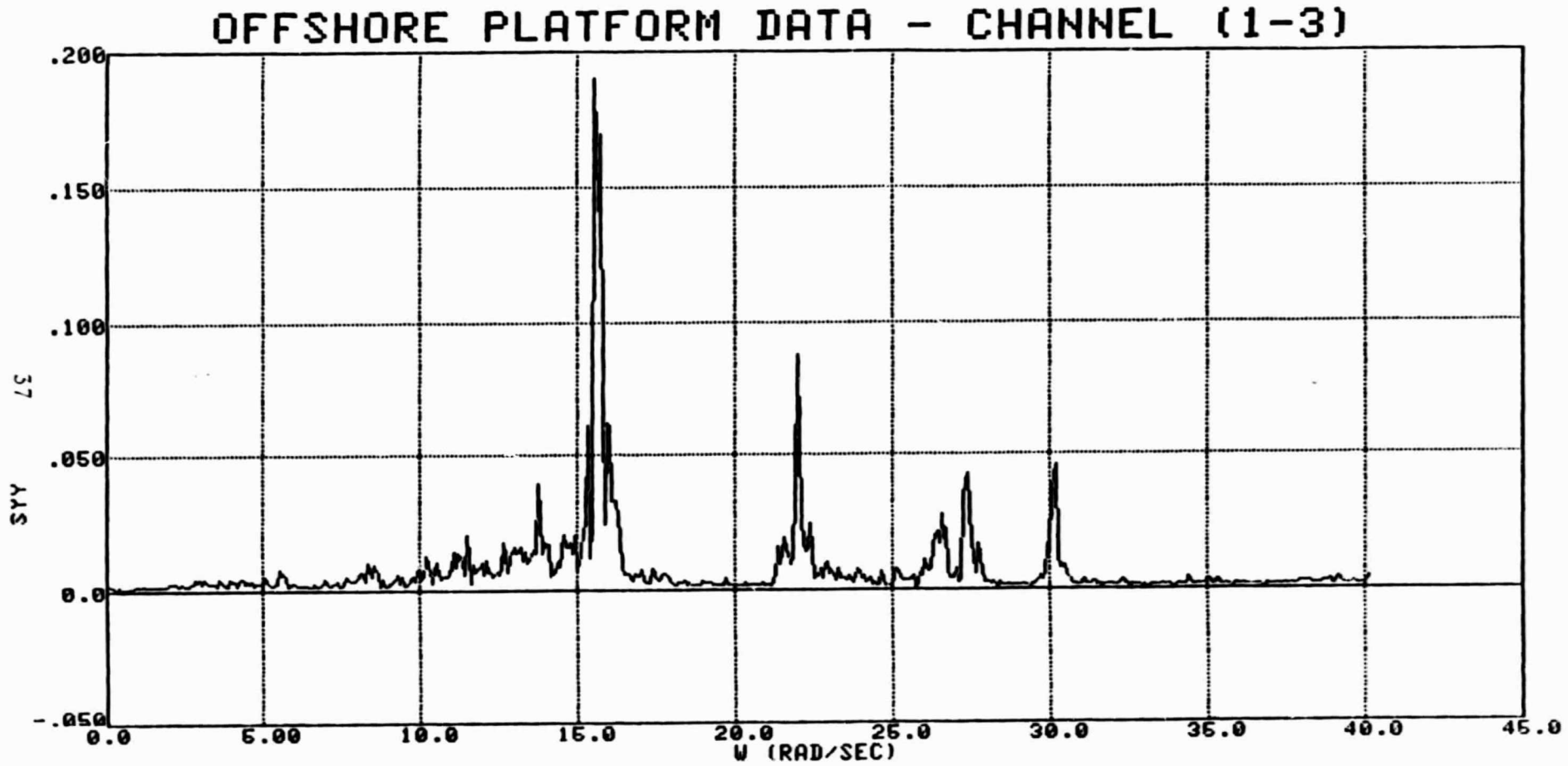

Figure 4.13c Spectrum of Rotational Acceleration

Table 4.6

Off-Shore Platform Modes

Comparison of Modes Identified by Maximum Entropy Method (MEM) [8] and Instrumental Variables Modal Estimation (IVME)

DIRECTION	THEORETICAL [18] F (Hz)	MEM [8]		IVME (1024 Data/Record)		IVME (2048 Data/Record)	
		F (Hz)	d (%)	F (Hz)	d (%)	F (Hz)	d (%)
x	2.37	2.19	.7	2.21	.8	2.21	.5
	3.60	3.40	.7	3.45	.7		
y	2.37	2.28		2.28	.9	2.27	.7
	3.61	3.44					
θ	2.81	2.49	.6	2.49	.7	2.50	.6
	3.90	3.50	.5	3.51	.5		
		4.23	.5				
		4.36		4.36	.1		
				4.81	.4	4.80	.1

movement, can alter the vibration modes and shapes significantly. Active control for LSS is, therefore, not only used for damping and attitude control, but also stiffening of the structure and shape control.

The problem of controlling a LSS is difficult because the dynamic model is infinite, whereas the physically realizable controller must be finite, both in space and the number of observations required. The finite dimensional model is generally determined by finite element modeling techniques and reduced for the control realization. Finite dimensional models generally only include the lowest order modes [20] and the modes close to excitations (machine vibrations, solar, magnetic, residual aerodynamic or gravity forces). As shown in Ref. 19, even for this radically reduced order system the poles and zeros are very closely placed. Even small misalignments and/or model uncertainty of the robust colocated sensor-actuator modal controller of Arbel [2] can therefore excite vibrational modes of the structure. The dynamic behavior of LSS, including the actuator and sensor systems must therefore be carefully identified before deciding on the best form of the controller, its structure, and its gains.

The effort here is to show the feasibility of identifying the modes and damping ratios of LSS by instrumental variables modal estimation. A simulation model of a space structure, designed by K. Soosaar and R. Strunce of Charles Stark Draper Laboratory (CSDL) (Figure 4.14) with damping provided by the low authority colocated controller of Ref. 2 is described by

$$\dot{x} = \begin{bmatrix} 0 & I_n \\ -A_o & B_o K B_o^T \end{bmatrix} x + \begin{bmatrix} 0 \\ B_o \end{bmatrix} u ,$$

where the squares of the modes of the open-loop system are

$$\text{diag } A_o = [1.8,\ 2.77,\ 8.36,\ 8.75,\ 11.5,\ 17.7,\ 21.7,\ 22.6,\ 72.9,\ 85.6,\ 106,\ 167]$$

the control distribution matrix is

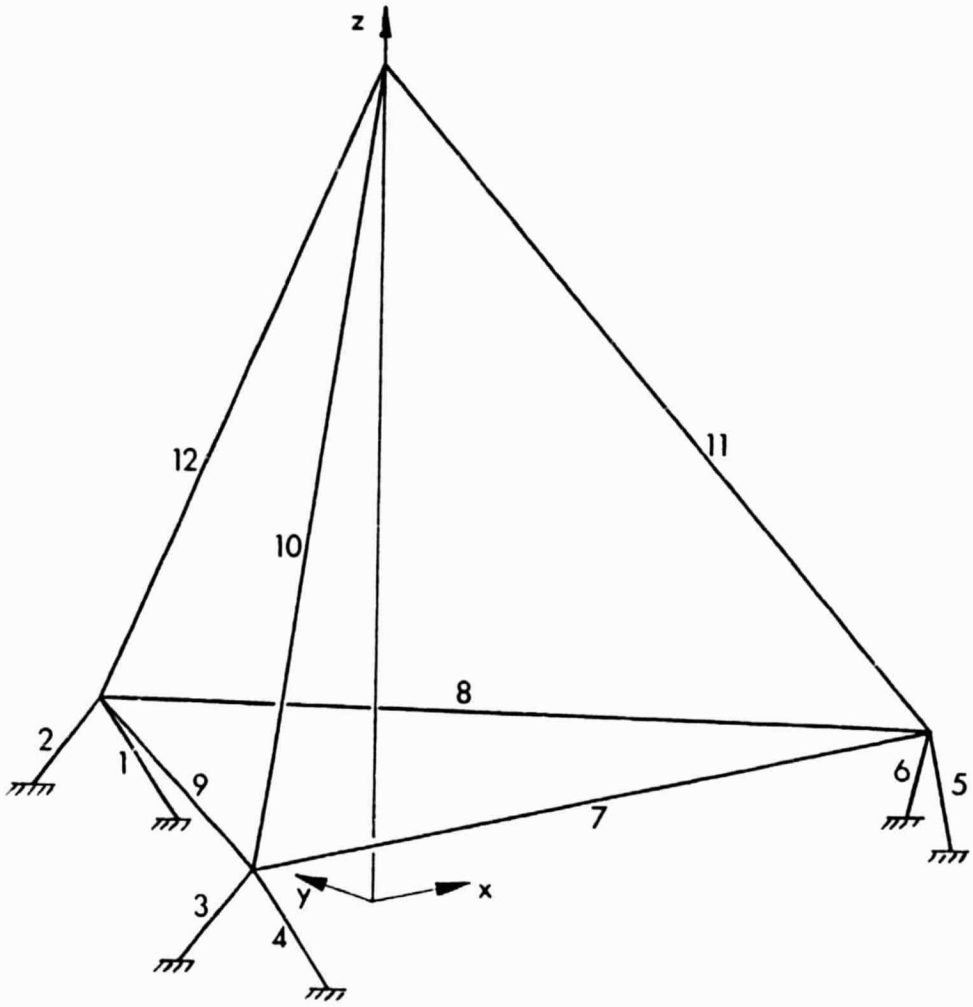

Figure 4.14 CSDL Space Structure Model

$$B_o = \begin{bmatrix} -.023 & -.067 & -.439 \\ -.112 & .017 & .069 \\ -.077 & .271 & .046 \\ .189 & -.060 & -.249 \\ .156 & -.049 & .351 \\ -.289 & .289 & -.289 \\ -.320 & -.369 & -.049 \\ .365 & .299 & -.069 \\ -.229 & .250 & .231 \\ .167 & -.150 & -.317 \\ -.145 & .146 & -.220 \\ .025 & -.013 & .114 \end{bmatrix}$$

and the control gain of the closed-loop system is

$$K = \begin{bmatrix} -12.43 & -0.506 & 3.129 \\ -0.506 & -7.591 & -5.199 \\ 3.129 & -5.199 & -12.82 \end{bmatrix}$$

The system was excited by a sinusoidal frequency sweep u. The measurements were corrupted by white noise. Figures 4.15a-ℓ show the transfer function measurements of the IVME algorithm, and Table 4.7 compares some of the actual and identified modes of the space structure. The dominating modes were identified with less than 1% error. The highly damped modes were poorly identifiable and resulted in larger errors up to 8% in frequency and 30% in damping ratio. Since the highly damped modes are naturally stable, they should not be considered in the reduced order model used for controller design. Hence, the poor behavior of the estimator for highly damped modes is of no practical concern.

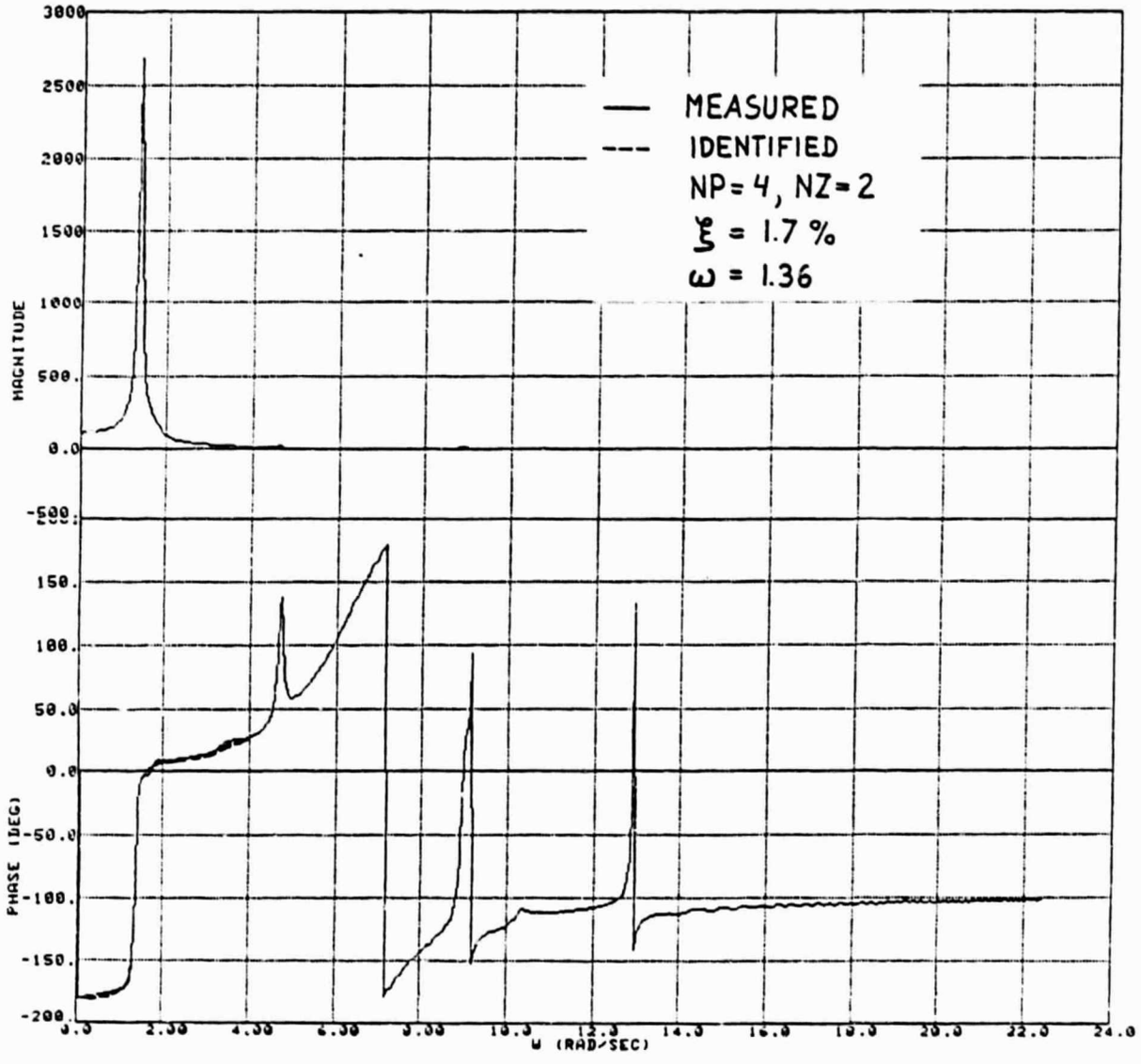

Figure 4.15a Measured and Identified Transfer Functions of State 1 of CSDL Pyram 1

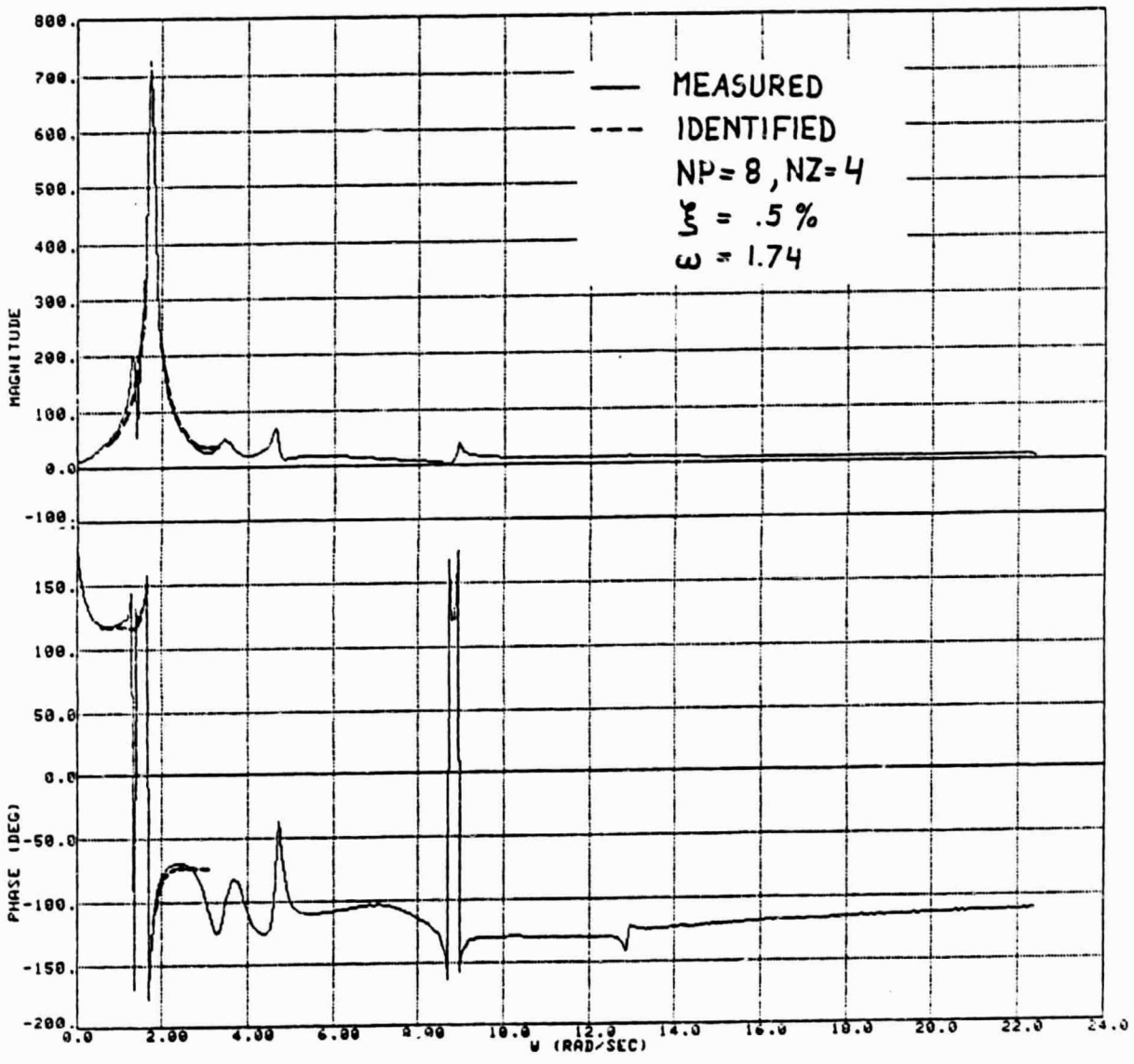

Figure 4.15b Measured and Identified Transfer Function of State 2 of CSDL Pyramid

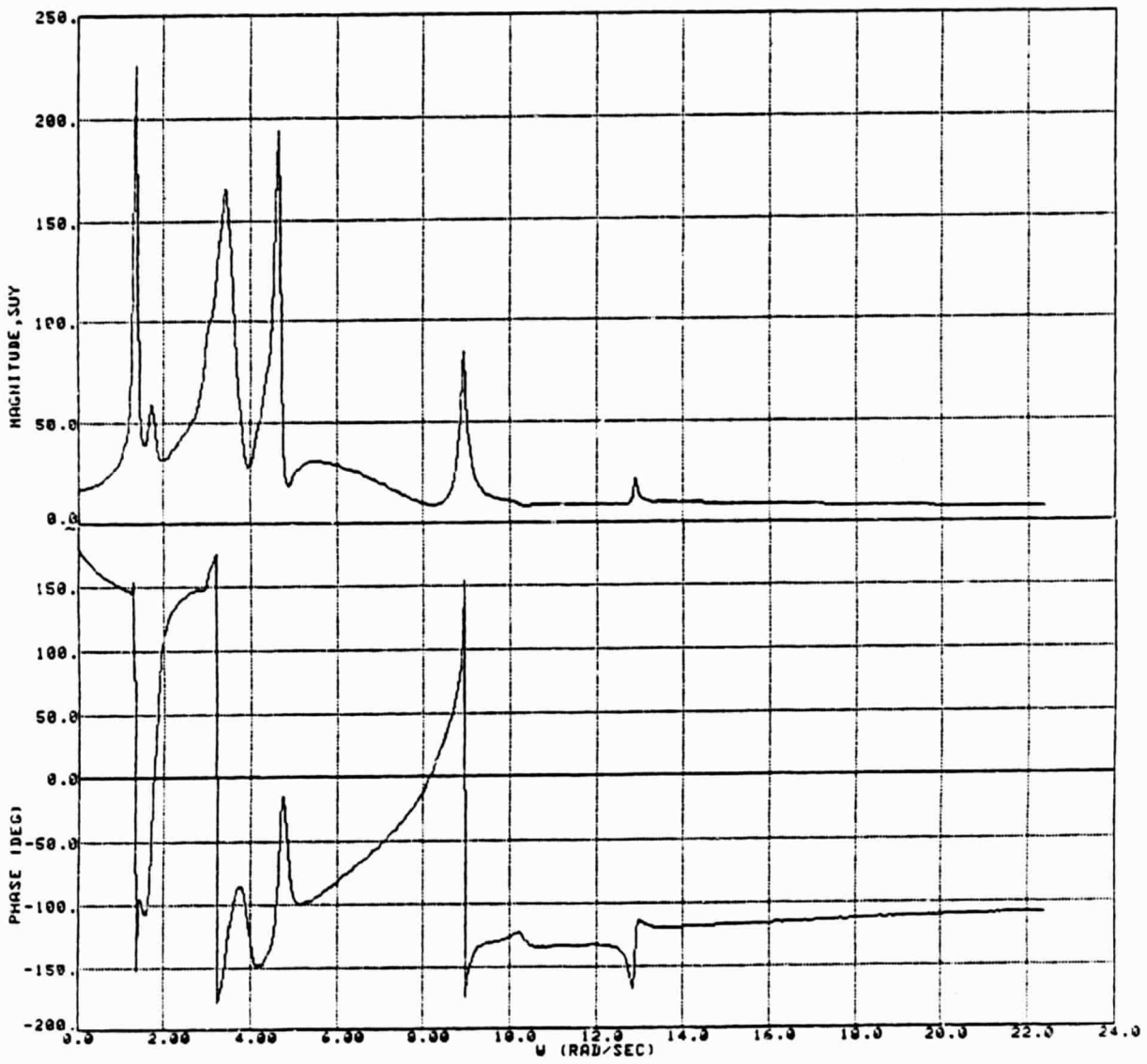

Figure 4.15c Measured Transfer Function of State 3 of CSDL Pyramid

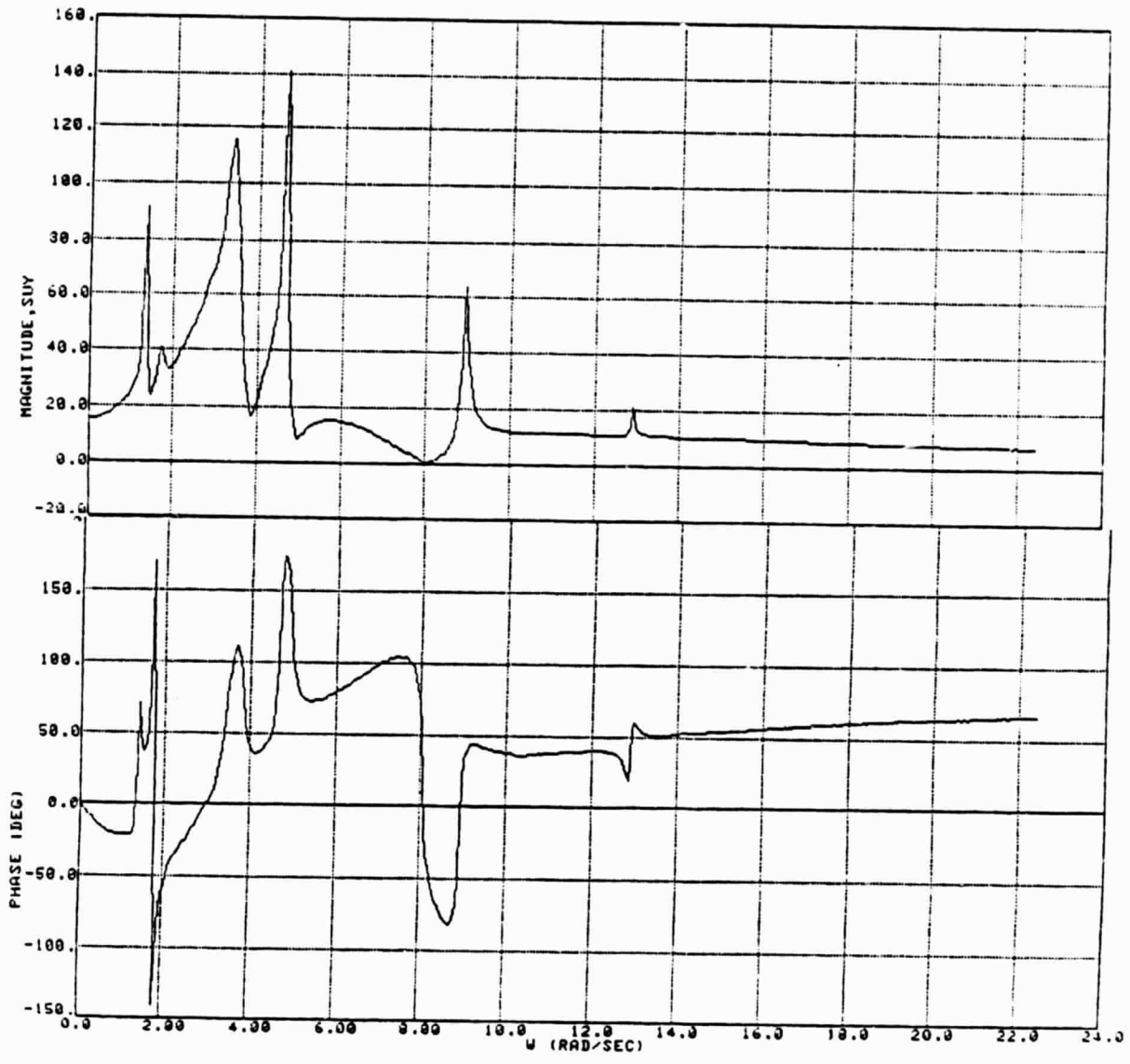

Figure 4.15d Measured Transfer Function of State 4 of CSDL Pyramid

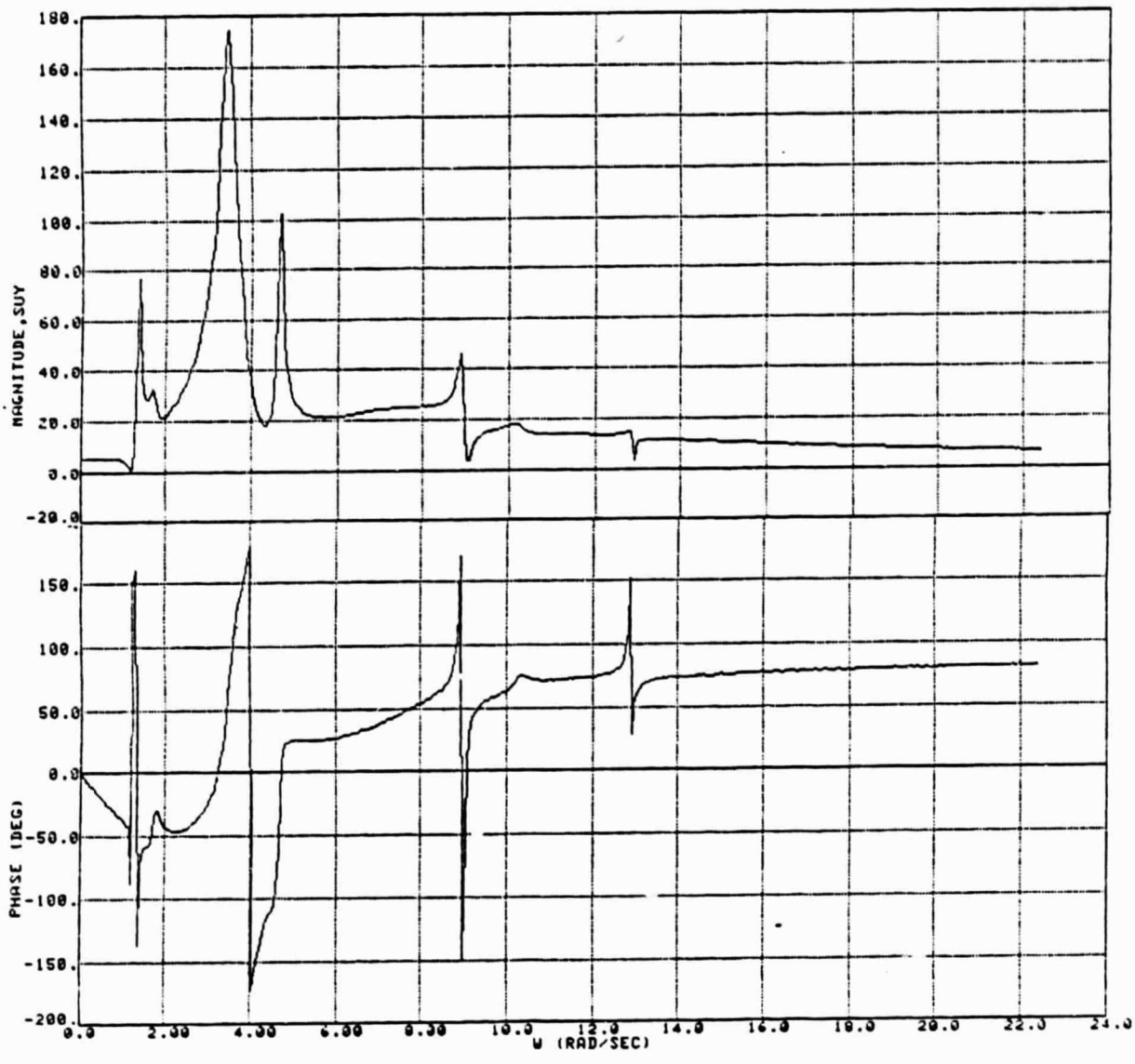

Figure 4.15e Measured Transfer Function of State 5 of CSDL Pyramid

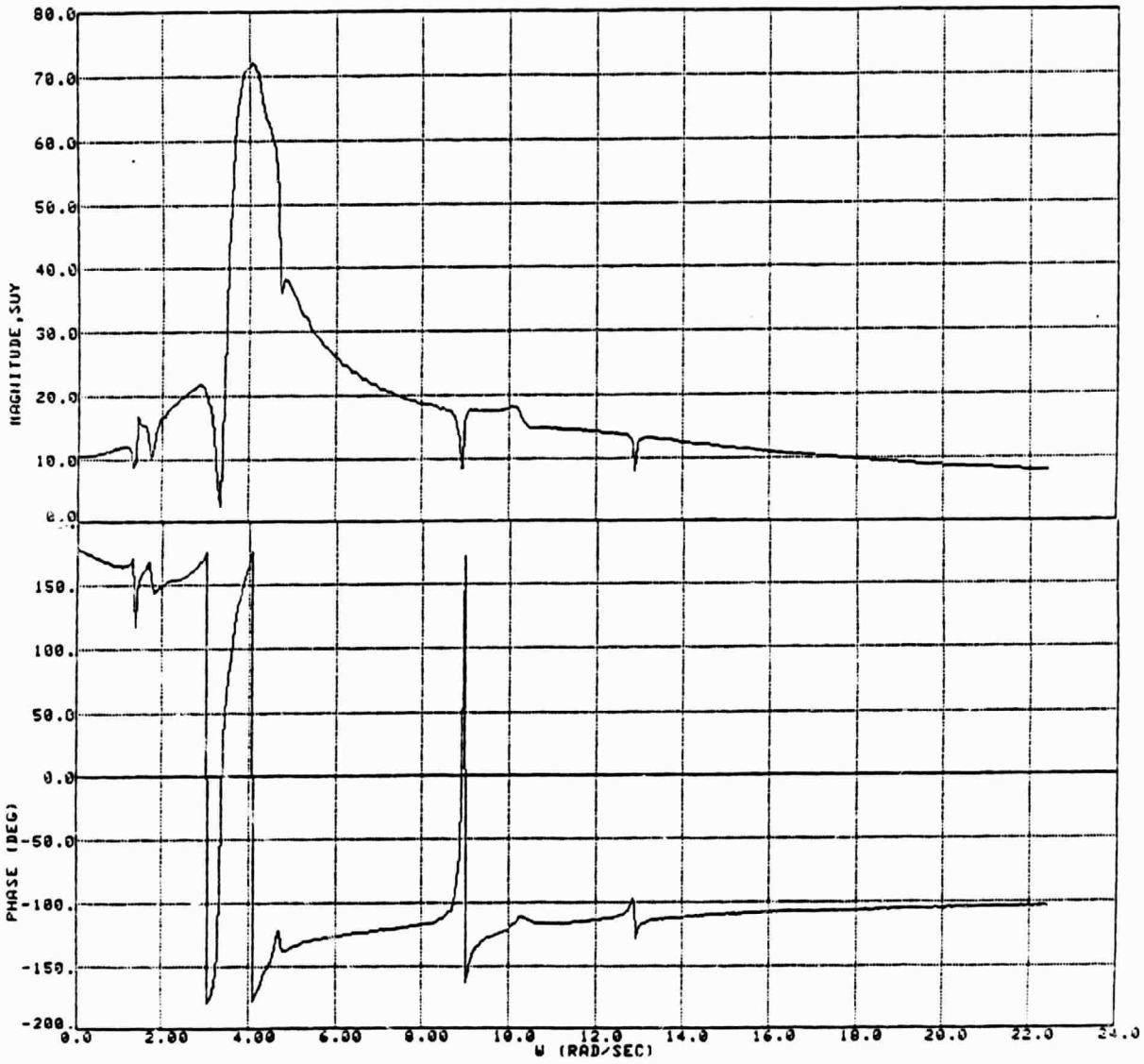

Figure 4.15f Measured Transfer Function of State 6 of CSDL Pyramid

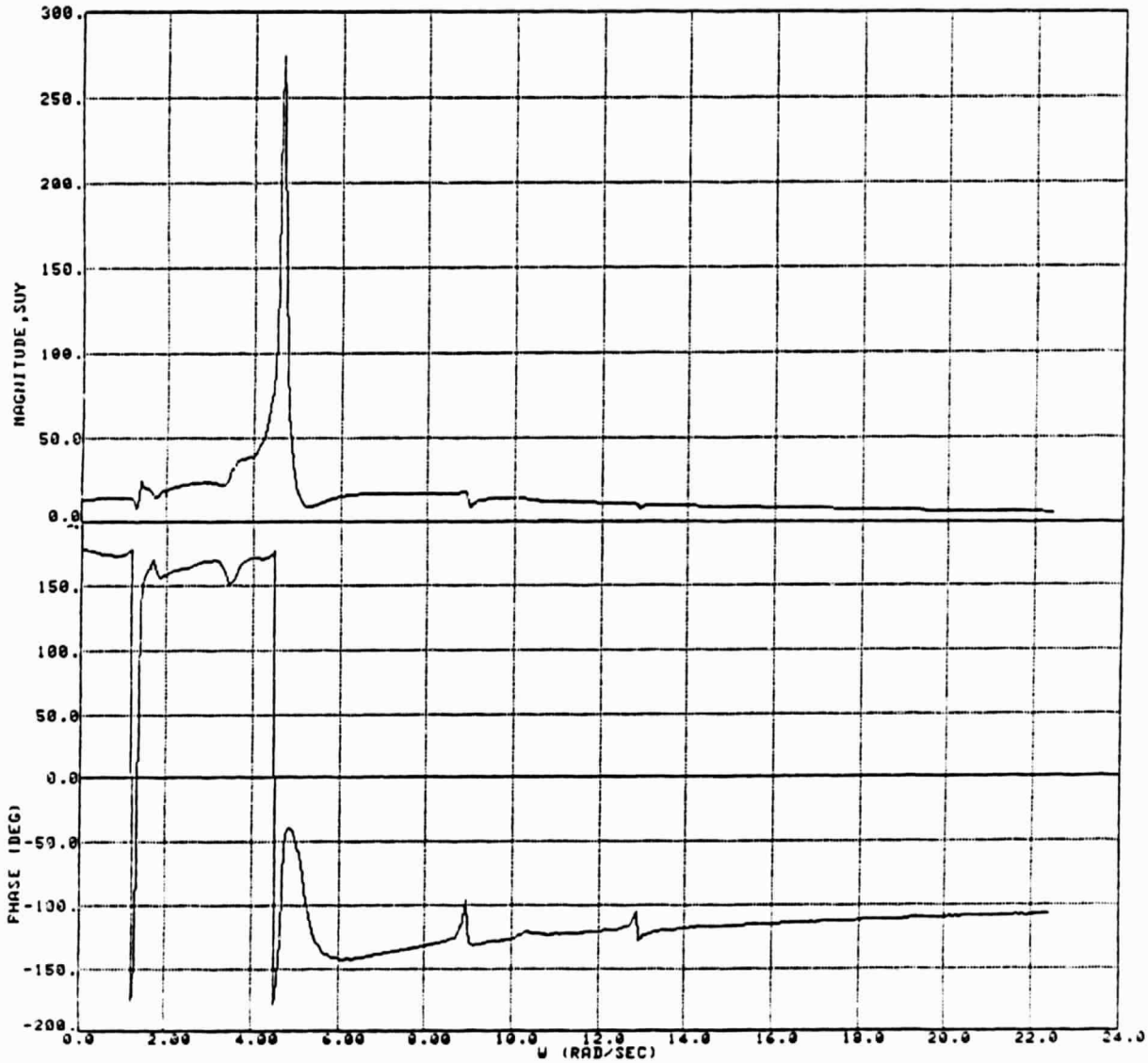

Figure 4.15g Measured Transfer Function of State 7 of CSDL Pyramid

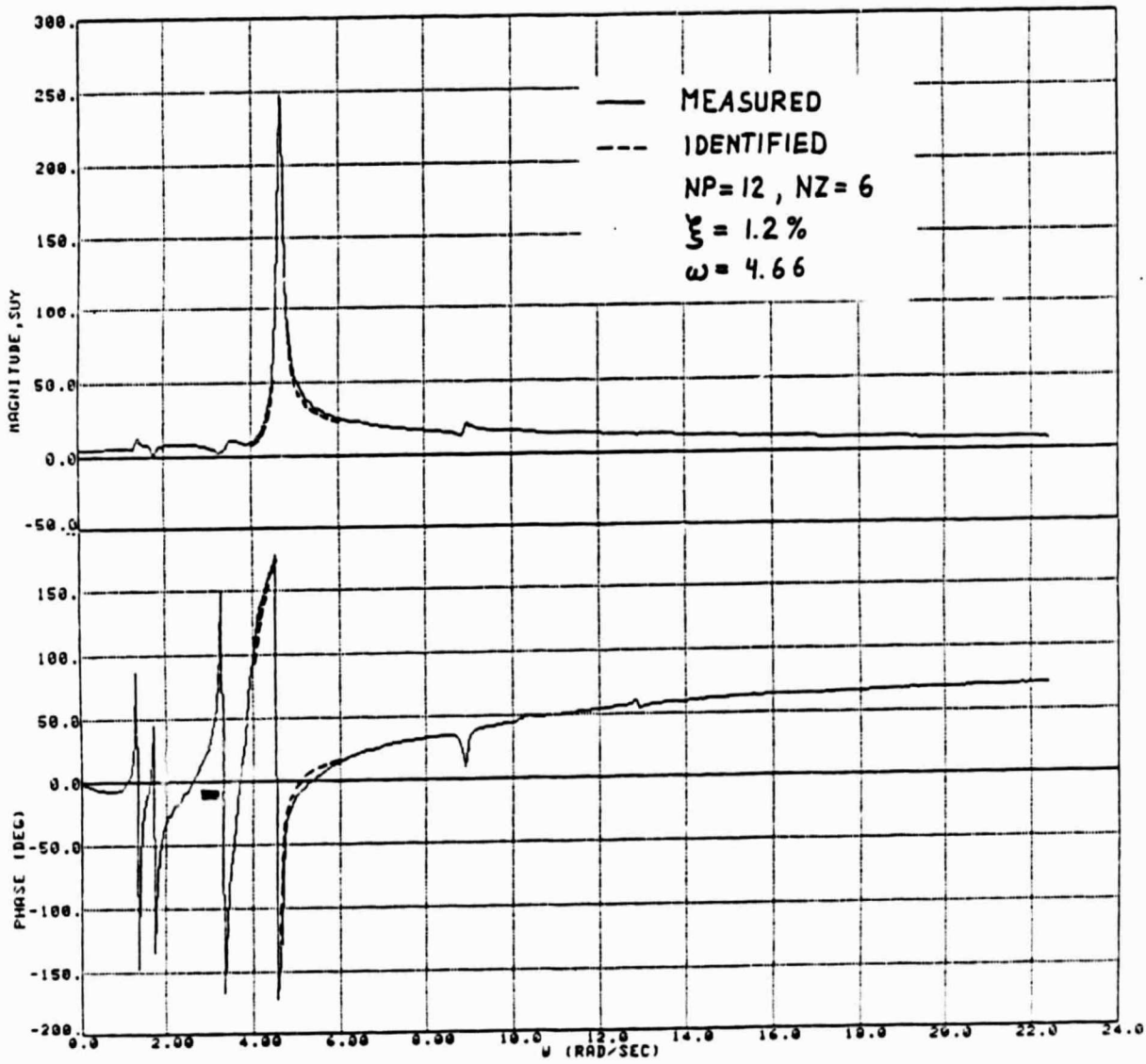

Figure 4.15h Measured and Identified Transfer Functions of State 8 of CSDL Pyramid

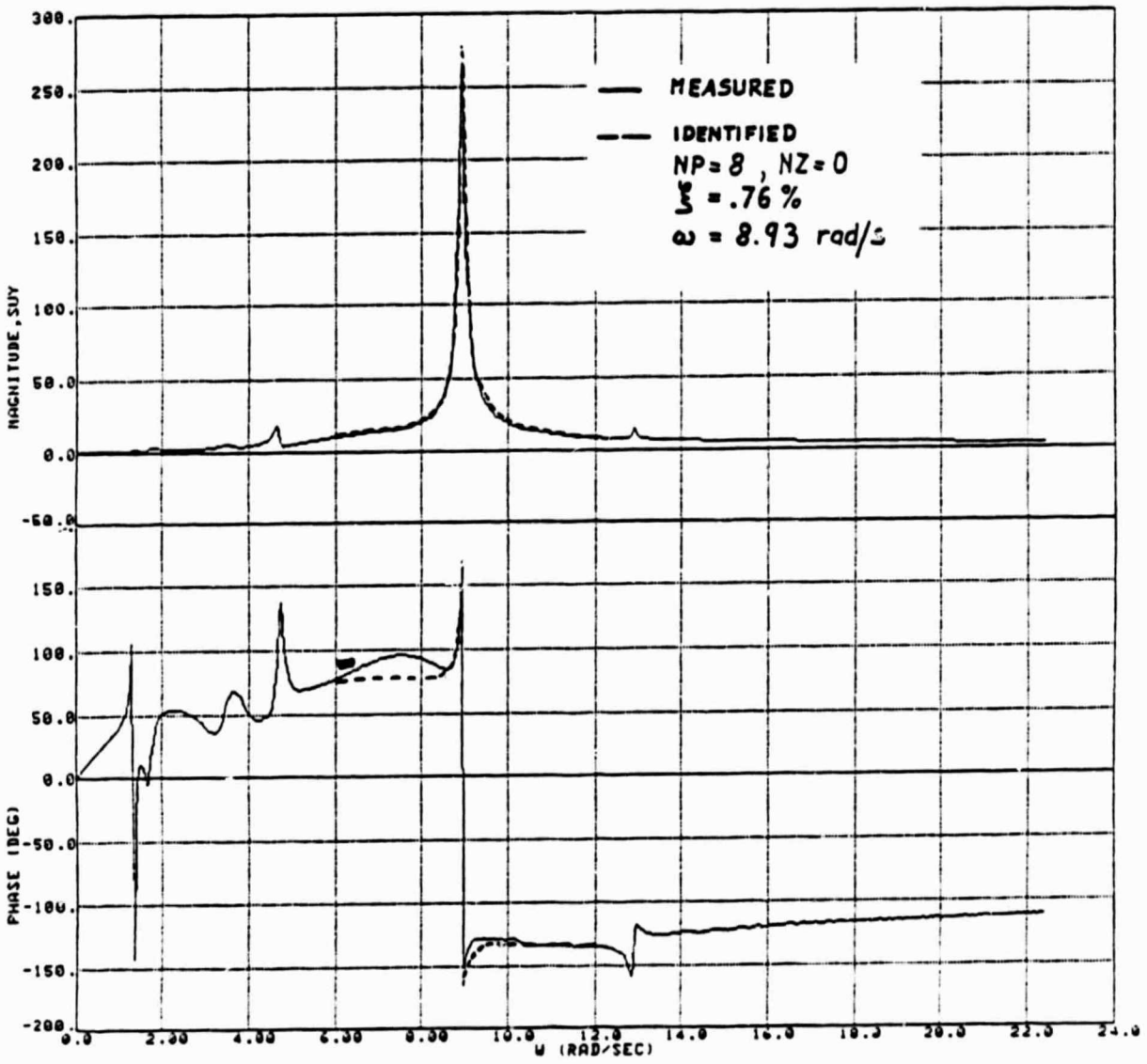

Figure 4.15i Measured and Identified Transfer Function of State 9 of CSDL Pyramid

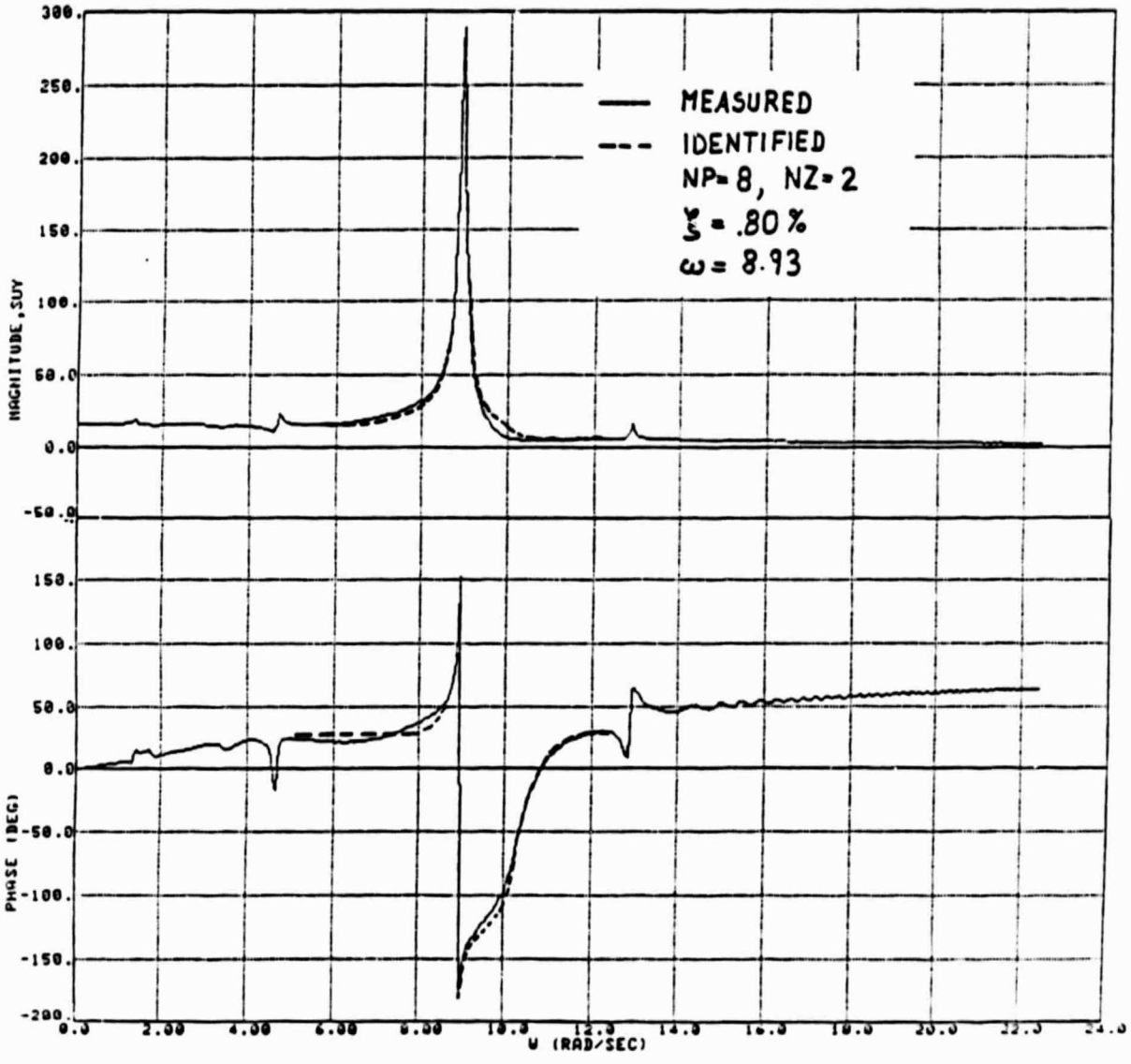

Figure 4.15j Measured and Identified Transfer Function of State 10 of CSDL Pyramid

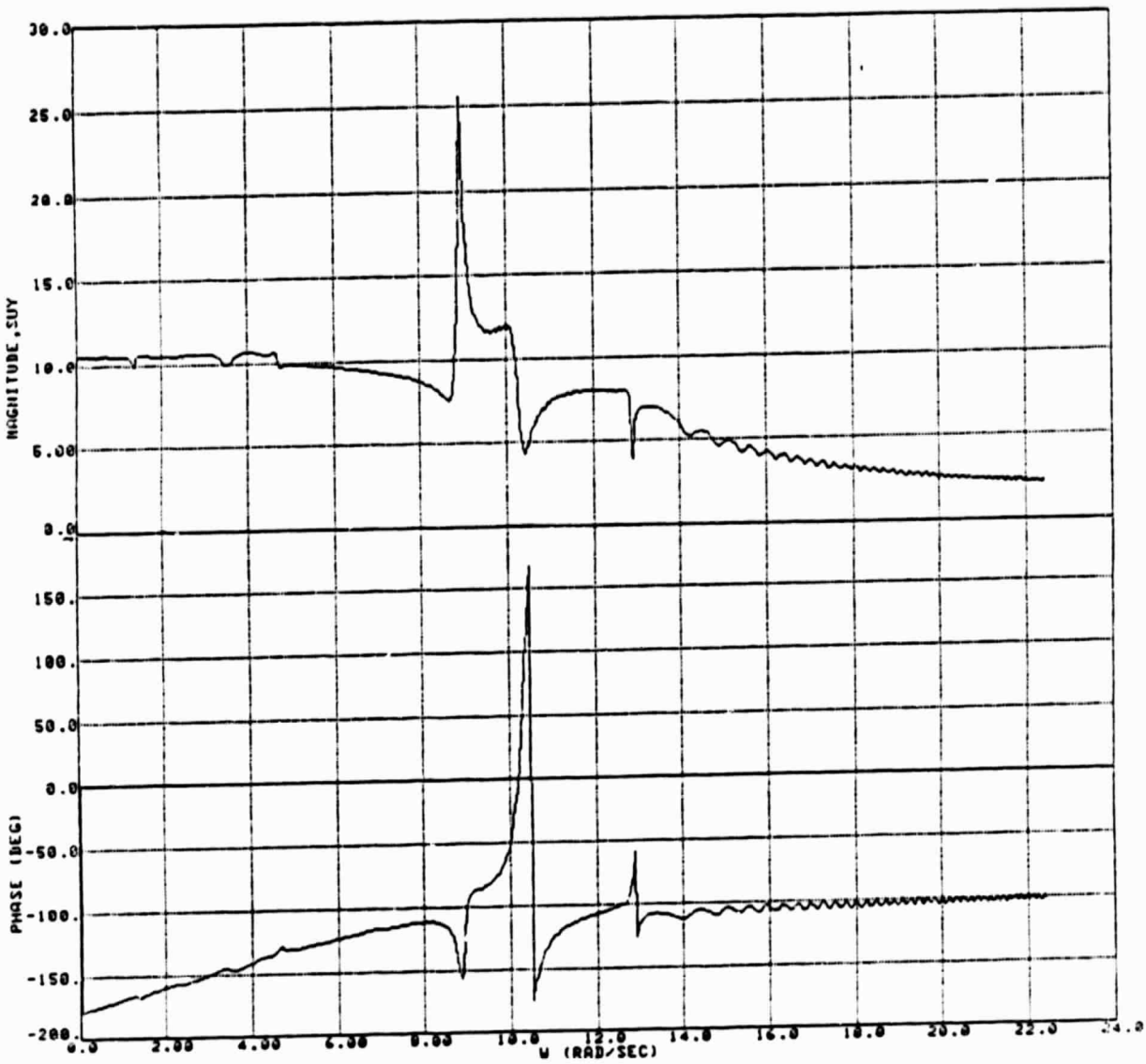

Figure 4.15k Measured Transfer Function for State 11 of CSDL Pyramid

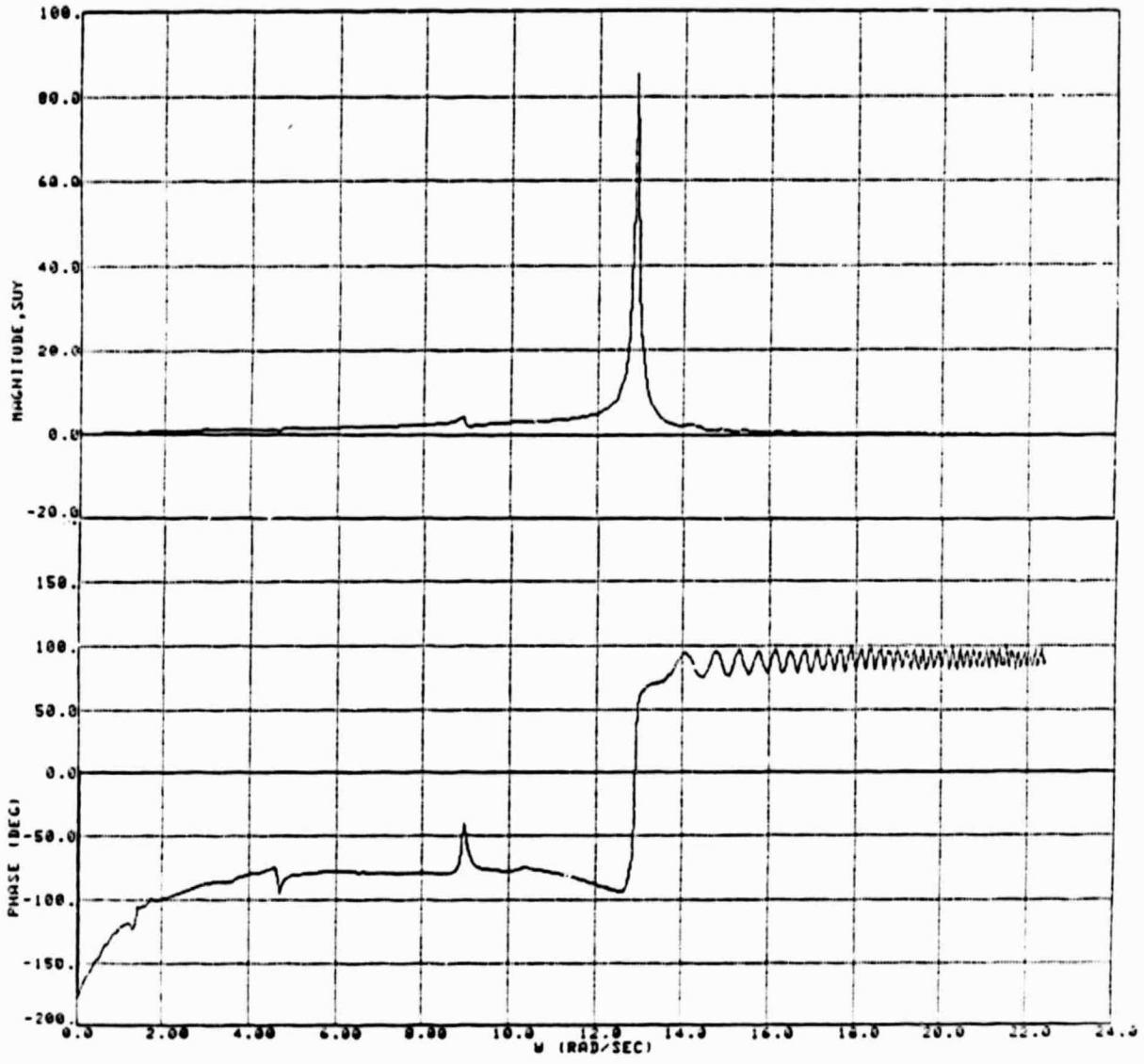

Figure 4.15ℓ Measured Transfer Function for State 12 of CSDL Pyramid

Table 4.7

Comparison of Theoretical and Identified Modes of CSDL Pyramid

MODAL STATE	FREQUENCY OF UNDAMPED SYSTEM	DAMPED SYSTEM		IDENTIFIED MODES	
		f	ζ[%]	f	ζ[%]
1	1.34	1.36	2.6	1.36	1.7
2	1.66	1.74	5.0	1.74	5.1
3	2.89	2.97	3.4		
4	2.96	2.76	60.5		
5	3.39	3.46	5.8		
6	4.21	4.07	13.9		
7	4.56	3.49	61.7		
8	4.75	4.66	1.3	4.66	1.2
9	8.54	7.25	26.7	8.93	.76
10	9.25	8.93	0.8	8.93	.80
11	10.3	10.23	2.0		
12	12.9	12.89	0.3		

REFERENCES

1. J.N. Aubrun, N.K. Gupta, M.G. Lyons, G. Margulies, "Large Space Structures Control: An Integrated Approach," AIAA Guidance and Control Conference, Paper 79-1764, 1979.

2. A. Arbel, "Robust Colocated Control for Large Flexible Space Structures," AIAA J. of Guidance and Control (forthcoming).

3. Proceedings of the 1958 Flight Flutter Testing Symposium, NASA SP-385, 1958.

4. Baird, E.F. and W.B.Clark, "Recent Developments in Flight Flutter Testing in the United States," AGARD Report 596, 1972.

5. Rosenbaum, R., "Survey of Aircraft Subcritical Flight Flutter Testing Methods," NASA CR-132479, 1974.

6. Houbolt, J.C., "Subcritical Flutter Testing and System Identification," NASA CR-132480, 1974.

7. Proceedings of NASA Symposium on Flutter Testing Techniques, NASA SP-415, 1975.

8. J.K. VanDiver and R.B. Campbell, "Estimation of Natural Frequencies and Damping Ratios of Three Similar Off-Shore Platforms Using Maximum Entropy Spectral Analysis," ASCE Spring Convention, Boston, April 1979.

9. J.K.VanDiver, "Prediction of the Damping Controlled Response of Off-Shore Structures to Random Excitation," 11th Annual Off-Shore Technology Conference, Houston, Texas, May 1979.

10. J.P. Burg, "Maximum Entropy Spectral Analysis," Ph.D. Thesis, Stanford University, May 1975.

11. Johnson, W., "Development of a Transfer Function for Dynamic Stability Measurement," NASA TN D-85522, July 1977.

12. N.K. Gupta and J.G. Bohn, "A Technique for Measuring Rotorcraft Dynamic Stability in the 40 by 80 Foot Wind Tunnel," NASA CR-151955, 1977.

13. H. Salzwedel and N.K. Gupta, "Identification of Dynamical Systems in the Presence of Non-Gaussian and Non-White Noise," Systems Control, Inc. (Vt) Report TR 5274-04, December 1979.

14. P.J. Huber, Robust Statistical Procedures, Society for Industrial and Applied Mathematics, Philadelphia, 1977.

55-56

15. W. Johnson and N.K. Gupta, "Instrumental Variables Algorithm for Modal Parameter Identification in Flutter Testing," AIAA Journal, Vol. 16, August 1978.

16. H. Akaike, "Stochastic Theory of Minimal Realization," IEEE Trans. Auto. Control, AC-19, December 1974.

17. E.Tse and H. Wienert, "Structure Determination and Parameter Identification for Multivariable Stochastic Linear Systems," IEEE Trans. Auto. Control, AC-20, October 1975.

18. B-52E CCV Flight Test Data Applicable to Parameter Estimation, AFFDL-TR-75-131.

19. G.D. Martin, On the Control of Flexible Mechanical Systems, SUDAAR 511, Department of Aeronautics and Astronautics, Stanford University, 1978.

20. R.J. Guyan, "Reduction of Stiffness and Mass Matrices," AIAA Journal, February 1965.

21. A. Arbel and N.K. Gupta, "Robust Generalized Colocated Control for Large Flexible Space Structures," Joint Automatic Control Conference, San Francisco, 1980.

22. J. Rissanen, "Minmax Entropy Estimation of Models for Vector Processes," R.K. Mehra and D.G. Laikiotis (Eds.), Systems Identification: Advances and Case Studies, Academic Press, 1976.

23. P.C. Young and A.J. Jakeman, "Refined Instrumental Variable Methods of Recursive Time-Series Analysis, Part I: Single Input/Single Output Systems," International Journal of Control, January 1979.

APPENDIX A
FREQUENCY DOMAIN ARMA EQUATIONS

A linear, time-invariant dynamic system of order n is described by a set of linear constant coefficient differential equations of the form

$$y^{(n)} + \sum_{i=1}^{n} a_i y^{(n-i)} = \sum_{i=1}^{m} b_i u^{(m-i)} + v \qquad (1)$$

where y is the output vector of dimension p, u is the input exciting the system, and the parameters a_i, i=1 to n and b_i, i=1 to m are the coefficients of the characteristic equations for the poles and zeros of the system, respectively. In the frequency domain, Eq. (1) may be written as

$$(j\omega)^n Y = Y [(j\omega)^{n-1} \ \ldots \ 1]\alpha + \begin{bmatrix} \beta_1^T \\ \vdots \\ \beta_p^T \end{bmatrix} \begin{bmatrix} (j\omega)^m \\ \vdots \\ 1 \end{bmatrix} U \qquad (2)$$

$$\alpha = [-a_n, \ \ldots \ -a_1)^T , \qquad \beta = [b_m, \ \ldots \ b_1]^T$$

where Y and U are the Fourier transforms of y and u. Premultiplying each of the p equations from Eq. (2) by

$$[(-j\omega)^{n-1} \ \ldots \ 1]^T \ Y_k^* e^{j\omega\tau} , \ k = 1 \text{ to } p \text{ and } [(-j\omega)^m \ldots 1]^T U^*$$

gives a set of $p(p-1)/2$ independent linear matrix equations

$$\Omega_{n-1} S_{y_{ki}} e^{j\omega\tau} = S_{y_{ki}} e^{j\omega\tau} \Omega_{n-1,n-1} \alpha + S^*_{uy_k} e^{j\omega\tau} \Omega_{n-1,m} \beta_k, \ k,i=1 \text{ to } p, \qquad (3)$$

and p equations,

$$\Omega_m S_{uy_k} = S_{uy_k} \Omega_{m,n-1} \alpha + S_{uu} \Omega_{m,m} \beta_k, \ k-1 \text{ to } p, \qquad (4)$$

where $S_{y_{ki}} = Y_k^* Y_i$, $S_{uy_k} = U^* Y_k$, $S_{uu} = U^* U$,

$$\Omega_{\ell} = \begin{bmatrix} j^{n-\ell}\ \omega^{n+\ell} \\ \vdots \\ j^{n}\omega^{n} \end{bmatrix} \quad ,{}^{\Omega}p,_{\ell} = \begin{bmatrix} j^{\ell-p}\omega^{p+\ell} \ldots & j^{-p}\omega^{p} \\ & \vdots \\ j^{\ell}\omega^{\ell} \quad \ldots & 1 \end{bmatrix}$$

Equations (3) and (4) are valid for all ω, and hence can be integrated over all ω or, in the case of discrete Fourier transforms, averaged. The average equations are,

$$V_{y_{ki}}(\tau) = M_{y_{ki}}(\tau)\alpha + M^{*}_{uy_k}(\tau)\beta_k, \quad k,i=1 \text{ to } p, \tag{5}$$

$$V_{uy_k} = M_{uy_k}\alpha + M_{uu}\beta_k, \quad k=1 \text{ to } p, \tag{6}$$

with

$$V_{y_i}(\tau) = \sum_{\omega} \Omega_{n-1} S_{y_{ki}} e^{j\omega\tau} ,$$

$$M_{y_{ki}}(\tau) = \sum_{\omega} S_{y_{ki}} e^{j\omega\tau} \Omega_{n-1,n-1},$$

$$M^{*}_{uy_k}(\tau) = \sum_{\omega} S_{uy_k} e^{j\omega\tau} \Omega_{n-1,m},$$

$$V_{uy_k} = \sum_{\omega} \Omega_{m} S_{uy_k},$$

$$M_{uy_k} = \sum_{\omega} S_{uy_k} \Omega_{m,n-1},$$

$$M_{uu} = \sum_{\omega} S_{uu} \Omega_{m,m},$$

$$\omega \varepsilon R_{\omega}$$

and R is the space of all significant frequencies.

These equations are non-singular if rank $(M_{uu})=m+1$, and rank $(M_{y_{ki}})= n$. For the case of zero input, equation (5) simplifies to

$$V_{y_{ki}}(\tau) = M_{y_{ki}}(\tau)\alpha \quad . \tag{7}$$

This equation defines the characteristic equation and poles of the system.

APPENDIX B

SOLUTION OF THE INSTRUMENTAL VARIABLES ARMA EQUATIONS

For a system with n poles, m zeros, p measurements and a scalar input u the equations defining the ARMA coefficients in the frequency domain are

$$V_{y_i}(\tau) = M_{y_{ki}}(\tau)\alpha + M^*_{uy_k}(\tau)\beta_k, \quad k,i=1 \text{ to } p \tag{1}$$

$$V_{uy_k} = M_{uy_k}\alpha + M_{uu}\beta_k, \quad k=1 \text{ to } p, \tag{2}$$

where $V(\tau)$ and $M(\tau)$ are defined by the auto and cross spectra of the input and output of the system respectively. τ is a time delay (see Appendix A). Solving Equation (2) for β_k gives

$$\beta_k = M_{uu}^{-1}[V_{uy_k} - M_{uy_k}\alpha], \quad k=1 \text{ to } p \tag{3}$$

and so

$$A_{ki}(\tau) = B_{ki}(\tau), \quad k,i=1 \text{ to } p, \tag{4}$$

with

$$A_{ki}(\tau) = M_{y_{ki}}(\tau) - M^*_{uy_k}(\tau)\, M_{uu}^{-1} M_{uy_k},$$

$$B_{ki}(\tau) = V_{y_{ki}}(\tau) - M^*_{uy_k}(\tau)\, M_{uu}^{-1}\, V_{uy_k}.$$

Using different τ, $\tau_{min} = 2n\Delta t$, results in $n_\tau * p^2$ independent equations for α. Combining these equations gives

$$A\alpha = B \tag{5}$$

with

$$A = \begin{bmatrix} A_{11} \\ \vdots \\ A_{pp} \\ \hline \vdots \\ A_{11} \\ \vdots \\ A_{pp} \end{bmatrix} \begin{matrix} \\ \\ \\ \\ \tau = \tau_1 \\ \\ \\ \\ \tau = \tau_n \\ \\ \end{matrix} \qquad B = \begin{bmatrix} B_{11} \\ \vdots \\ B_{pp} \\ \hline \vdots \\ B_{11} \\ \vdots \\ B_{pp} \end{bmatrix} \begin{matrix} \\ \\ \\ \\ \tau = \tau_1 \\ \\ \\ \\ \tau = \tau_n \\ \\ \end{matrix}$$

The least squares solution of Equation (5) is

$$\alpha = (A^T A)^{-1} A^T B. \qquad (6)$$

Using α in equation (3) gives β_k, k=1 to p.

APPENDIX C

AVERAGING SOLUTION OF THE INSTRUMENTAL VARIABLES ARMA EQUATIONS

For a system with n poles, m zeros, p measurements and a scalar input u the equations defining the ARMA coefficients and β in the frequency domain are:

$$V_{y_{ki}}(\tau) = M_{y_{ki}}(\tau)\alpha + M^{*}_{uy}(\tau)\beta_k, \quad i=1 \text{ to } p, \tag{1}$$

$$V_{uy_k} = M_{uy_k}\alpha + M_{uu}\beta_k, \quad k=1 \text{ to } p, \tag{2}$$

where V and M are defined by the auto and cross spectra of input and output of the system respectively. τ is a time delay (see Appendix A).

The sum of Equations (1) is

$$\sum_{i,k,} V_{y_{ki}}(\tau) = \left[\sum_{i,k,\tau} M_{y_{ki}}(\tau)\right]\alpha + p \sum_{k}\left[\sum_{\tau} M^{*}_{uy_k}(\tau)\right]\beta_k. \tag{3}$$

Solving Equation (2) gives

$$\beta_k = M_{uu}^{-1}\left[V_{uy_k} - M_{uy_k}\alpha\right], \quad k=1 \text{ to } p, \tag{4}$$

and so

$$\left[\sum_{i,k,\tau} M_{y_{ki}}(\tau) - p\sum_{k}\left[\sum_{\tau} M^{*}_{uy_k}(\tau)\right] M_{uu}^{-1} M_{uy_k}\right]\alpha = \sum_{i,k,} V_{y_{ki}}(\tau) - p\sum_{k}\left[\sum_{\tau} M^{*}_{uy_k}(\tau)\right] M_{uu}^{-1} V_{uy_k} \tag{5}$$

or $C\alpha=d$. The solution is $\alpha=C^{-1}d$, from which β_k can be calculated using Equation (4).